ACS EARTH AND SPACE CHEMISTRY

http://pubs.acs.org/journal/aesccq

Article

Effect of EDTA Complexation on the Kinetics and Thermodynamics of Uranium Redox Reactions Catalyzed by Pyrite: A Combined Electrochemical and Quantum-Mechanical Approach

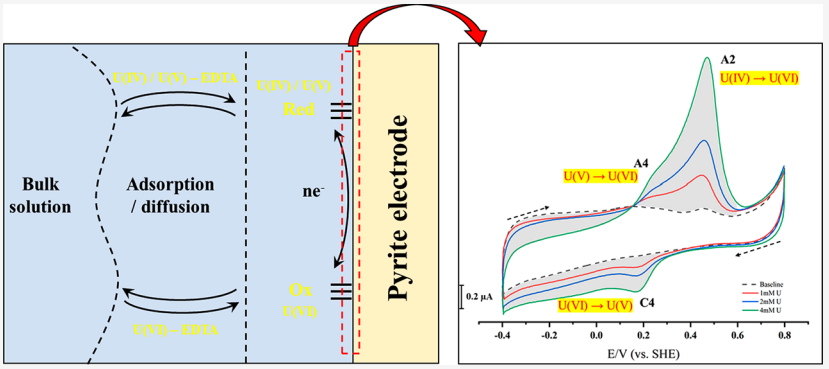
Yingwei Wang, Sooyeon Kim, Maria C. Marcano, Yijun Cao, and Udo Becker*

Cite This: *ACS Earth Space Chem.* 2022, 6, 830−846

Read Online

ACCESS | Metrics & More | Article Recommendations | Supporting Information

Downloaded via EGE UNIV on February 17, 2023 at 17:17:10 (UTC).
See https://pubs.acs.org/sharingguidelines for options on how to legitimately share published articles.



ABSTRACT: Ethylenediaminetetraacetic acid (EDTA), a strong complexing agent, is a common constituent of liquid nuclear waste streams. The interaction of EDTA or other organic or inorganic ligands with uranyl enhances the mobilization of uranium and therefore significantly influences the disposal and remediation of uranium waste. Although numerous studies have focused on the effect of EDTA on the mobilization of environmental uranium, including the adsorption and redox reactions of uranium on mineral surfaces, few studies have differentiated the reaction-controlling steps (diffusion, adsorption, and chemical reaction/electron transfer) occurring at heterogeneous interfaces to assess the effect of EDTA complexation on each of these processes. Here, a combination of in situ electrochemical methods and quantum-mechanical calculations was used to study the effect of EDTA complexation on the kinetics and thermodynamics of redox reactions of uranium at the pyrite-solution interface. Experiments indicate a potential shift of U(VI)/U(V) on the pyrite surface of ∼0.04 V due to surface adsorption and −0.21 V due to EDTA complexation, with similar results from the calculations. The oxidation of the U(IV) reaction is more sensitive to EDTA complexation in solution than that of U(V). Disproportionation, affecting 2/3 of the intermediate pentavalent state, is the rate-limiting step of the overall redox cycle of uranyl. The charge transfer was controlled by diffusion and adsorption processes. EDTA can promote the delivery of free uranyl from the bulk solution to the pyrite−water interface where the reaction takes place, making the electron-transfer process less diffusion-limited. Adsorption of uranyl onto pyrite surfaces in the gradient electric field is multimolecular layer adsorption, through which electron transfer can occur.

KEYWORDS: *ethylenediaminetetraacetate (EDTA), pyrite catalysis, uranium redox, electrochemistry, quantum-mechanical calculations*

1. INTRODUCTION

Ethylenediaminetetraacetic acid (EDTA) is a stable and strong complexing agent[1] that has been widely used in industrial cleaning, wood pulp bleaching, pharmaceutical production, manufacturing of textile, leather, and rubber, preparation of fertilizer and herbicide, and decontamination operations at nuclear facilities.[2−6] The progressively increasing amount of EDTA in the environment and EDTA from separation operations significantly influences the solubility and transport of actinyl ions during the geologic disposal and storage of radioactive wastes.[7,8] It has been reported that EDTA is a common ingredient of liquid nuclear waste streams, e.g., in the high-level nuclear waste-disposal trenches near Richland, Washington,[9,10] and uranium released to the environment with such waste streams is associated with EDTA complexes.[11] The interaction of EDTA with uranium enhances its mobilization, posing a risk to the long-term storage of nuclear wastes.[12,13]

Special Issue: Hochella Honorary

Received: November 27, 2021
Revised: March 6, 2022
Accepted: March 9, 2022
Published: March 15, 2022



ACS Publications

© 2022 American Chemical Society

Uranium is a redox-sensitive radionuclide, and its solubility is highly controlled by its oxidation states, of which U(IV) and U(VI) are the predominant uranium oxidation states in natural environments.[14] U(VI) in solution mainly exists as the uranyl cation (UO_2^{2+}) with high solubility and mobility. It also occurs in minerals such as studtite ($((UO_2)O_2(H_2O)_2{\cdot}2H_2O)$, where O_2^{2-} stands for the peroxide ion, which is a rare occurrence in mineral; metastudtite, schoepite ($((UO_2)_8O_2(OH)_{12}{\cdot}12H_2O)$, betafite ($((Ca,U)_2(Ti,Nb,Ta)_2O_6(OH))$, and uranophane ($Ca(UO_2)_2(SiO_3OH)_2{\cdot}5H_2O$). U(IV) commonly exists in sparingly soluble forms, such as uraninite (UO_2).[15,16] Thus, reducing soluble U(VI) to insoluble U(IV) compounds has been widely proposed as an effective remediation strategy for U-contaminated sites.[17−19] A growing body of studies has documented that U(V) as an intermediate is obtained by a fast one-electron reduction of UO_2^{2+} to UO_2^{+} on mineral surfaces, followed by disproportionation to U(IV) and U(VI) species.[20−25] During this process, mineral surfaces play a crucial role in stabilizing redox species.[26,27] Mineral surfaces can also promote the redox process by providing nucleation or adsorption sites for redox-active species, helping in the (partial) dehydration of fully hydrated species in solution and providing a substrate for the redox pair to meet via surface diffusion.[28] In addition, semiconducting sulfide and oxide surfaces can catalyze the actual electron transfer by allowing electron transfer to occur over tens of angstroms, a much longer distance than electron transfer in bulk water.[29] Thus, where an individual subprocess (i.e., approach, dehydration or decomplexation, and actual electron transfer) can be the obstacle in the overall redox process, a surface can act on one or more of these to help lower the activation energy of the overall reaction or facilitate electron transfer via an electron shuttle through the surface.[30−34] Recent spectroscopic studies have demonstrated that the reduction of U(VI) proceeds first through surface-associated U(VI) to form U(V).[35,36]

Redox reactions of radionuclides or other trace metals with different oxidation states are often accompanied by the participation of minerals in natural aqueous environments. Pyrite, a well-known natural semiconducting mineral,[37] is the most widespread sulfide mineral in geologic environments.[38] Because of its narrow bandgap, which gives it unique electronic characteristics that are distinct from those of insulating minerals or wide-bandgap semiconductors such as hematite,[30,31] pyrite was chosen as the reaction-mediating mineral for this study. In addition, the disulfide units have a more localized molecular character within the delocalized states close to the Fermi level. Another feature of pyrite is that Fe in the bulk is low-spin ferrous iron, while surface Fe can be in the low-, intermediate-, or high-spin state.[39]

Usually, work on the effect of EDTA on the mobilization of environmental uranium has focused on the adsorption/desorption of uranium on mineral surfaces. Rihs et al. studied the adsorption of U(VI) onto calcite surfaces in the presence of EDTA; they found that EDTA enhances the surface roughness of calcite by complexing and dissolving surface Ca^{2+} ions, thereby causing an increase of U(VI) adsorption.[9] Luo and Gu studied the effects of complexing organic ligands (citrate and EDTA) on the mobilization of uranium in a strict anaerobic environment and concluded that both EDTA and citrate could effectively cause the dissolution of reduced U(IV).[40] Zhao et al. used EDTA-functionalized Fe_3O_4/graphene oxide to remove U(VI) from aqueous solutions and showed its strong sorption capacities toward U(VI), as well as its good reusability and high stability.[41] Pshinko et al. used LDHs (layered double hydroxides) intercalated with EDTA to recover U(VI) from aqueous media and showed that LDHs intercalated with EDTA exhibit high adsorption performance for U(VI).[42] Some studies have addressed the effect of EDTA on the redox transformations of uranium species. Kim et al.[43,44] and Cerrillos et al.[45] demonstrated the photocatalytic reduction of U(VI) on anatase surfaces simultaneously with the oxidation of EDTA complexes in which U(VI) acts as the electron acceptor and EDTA acts as the electron donor. In these experiments, the ratio of U to EDTA controlled the reactivity of U(VI), and the production rate of U(IV) decreased with increasing EDTA concentration for the U/EDTA ratio up to 1:4. It was thought that uranyl−EDTA complexes such as $[(UO_2^{2+})HEDTA]^{-}$ compete with uncomplexed U(VI) for surface sites on the TiO_2 nanoparticles, hindering the photoreduction of uranyl. Sheng et al.[46] used microbes (*Shewanella oneidensis* MR-1) as the reductant in kinetics experiments on U(VI) reduction in the presence of varying concentrations of EDTA. In their experiments, the rate of U(IV) production increased with increasing EDTA concentration. While there seems to be a discrepancy in the literature as to whether EDTA promotes or hinders uranyl reduction, it appears that there may be a significant difference in the reduction mechanism and the involvement of EDTA depending on whether microbes are involved in the redox process. EDTA can act as carbon source for the microbes and aid in electron shuttling, thereby promoting electron transfer. In contrast, steric hindrance by the ligand limits the reaction with a reductant by curbing adsorption and, therefore, reduction if the redox process takes place on a sulfide or oxide surface. In this context, it may be misleading to explain experiments in the presence of microbes just using inorganic arguments.

Macroscopic batch experiments involving surfaces based on solution analysis and spectroscopic methods can help us understand the overall kinetics. Still, there are some unresolved questions about the mechanisms due to the complex heterogeneous-interface reaction process, generally involving three reaction-controlling steps: (i) diffusion in solution toward the surface, (ii) adsorption (often accompanied by surface diffusion as an outer-sphere or inner-sphere complex and transition from an outer- to inner-sphere complex), and (iii) chemical reaction including electronic transfer.[47−49] Few studies have differentiated the three subprocesses for heterogeneous reactions.[50−54]

In this study, a combination of electrochemical methods and quantum-mechanical calculations are used to study the effect of EDTA complexation on the kinetics of uranium redox reactions mediated by pyrite surfaces. The electrochemical approach involves a pyrite-powder microelectrode,[20,21,33,55] not only to evaluate uranium redox processes occurring in situ under various solution conditions but also to control the reaction rate of uranium species by changing the scan rate of the electrochemical potential. This helps estimate the effect of EDTA complexation on the redox reaction rate of uranium on the pyrite surface. The theoretical results, if they conform to the experiment, will strengthen the understanding of the mechanism of EDTA complexation and adsorption onto pyrite for U species with different oxidation states.

The objectives of this study are to (1) measure the redox reactions of pyrite in the background electrolyte, whose cyclic voltammetry (CV) curves will be used as the baseline; (2)

https://doi.org/10.1021/acsearthspacechem.1c00417
ACS Earth Space Chem. 2022, 6, 830−846

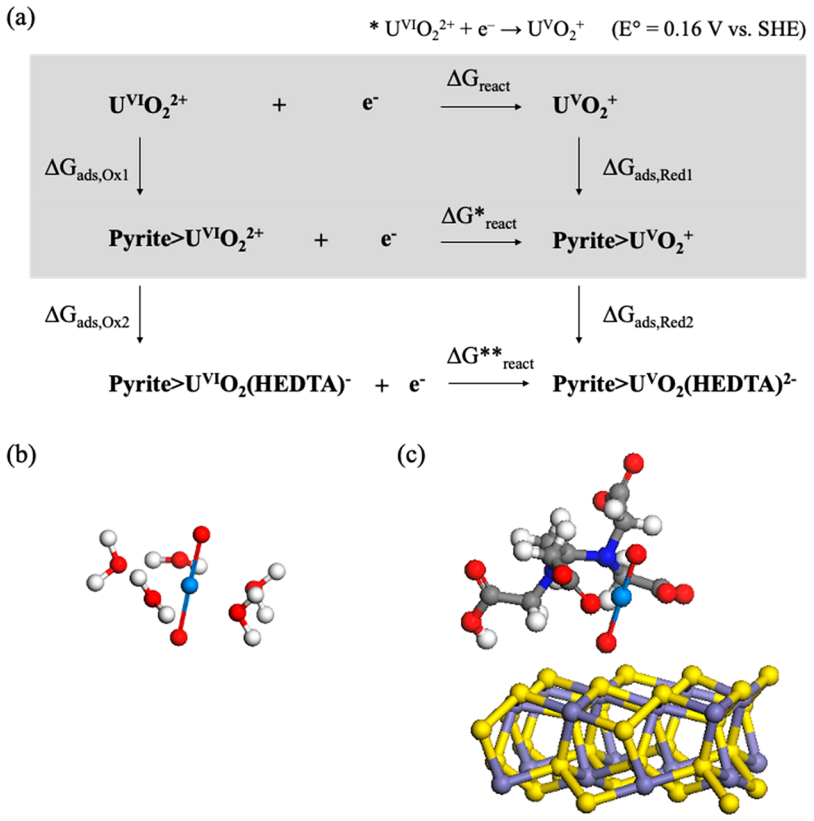


Figure 1. (a) Thermodynamic cycle for calculating Gibbs free energies of surface-adsorbed uranium species on the pyrite surface. Relations inside the gray box show redox reactions of free uranyl species and uranyl adsorbed to the pyrite surface. Reactions outside the gray box show the thermodynamic relations of the surface-adsorbed uranyl−HEDTA redox reaction. Because absolute values for the electrochemical potential are difficult to obtain accurately in a purely computational way, relationships between ΔG_{react} (this Gibbs free energy corresponds to the standard reduction potential), $\Delta G_{ads,Ox}$, and $\Delta G_{ads,Red}$ are used according to eqs 1−3, and ΔG^*_{react} is the resulting key entity for calculating the shifted electrochemical potential. (b, c) Model structures used in these calculations: (b) aquo-complexed free uranyl and (c) uranyl−HEDTA adsorbed on the pyrite surface. Blue, U; white, H; red, O; gray, C; dark blue, N; steel blue, Fe; and yellow, S.

measure the redox reactions of uranium on pyrite surfaces and evaluate the redox mechanism of uranium on pyrite surfaces; (3) examine the effect of EDTA complexation on the shift of the uranium redox potential on the pyrite surface and compare the reaction sensitivity of U(IV) and U(V) to EDTA in solution; and (4) investigate the effect of EDTA complexation on the reaction steps, including diffusion and adsorption. The findings presented herein are crucial to understanding the redox behavior of uranyl in the presence of EDTA (and the methodology could be transferred to other organic compounds in the environment or waste streams), which plays a significant role in the fate of uranium in the environment.

2. METHODS

2.1. Materials. Reagent-grade pyrite (FeS_2, Sigma-Aldrich, St. Louis, U.S.A.) was used instead of natural pyrite samples due to composition variability associated with a high density of inclusions typically found in natural samples. XRD patterns of purchased pyrite and standard pyrite (PDF no. 71-2219) confirm the high purity of the pyrite powder used (Figure S1). Pyrite powder with 14.51 ± 0.09 μm mean grain size determined by a laser particle size analyzer (MICROTRAC S3500, Microtrac, U.S.A.) was obtained by grinding and sieving in an anaerobic glovebox to avoid oxidation. Potassium chloride (KCl, reagent grade, Fisher Chemical), uranyl nitrate hexahydrate ($UO_2(NO_3)_2{\cdot}6H_2O$, reagent grade, International Bioanalytical Industries), ferrous chloride tetrahydrate ($FeCl_2{\cdot}4H_2O$, reagent grade, Fisher Chemical), and ethylenediaminetetraacetic acid (EDTA) disodium salt dihydrate ($C_{10}H_{14}N_2Na_2O_8{\cdot}2H_2O$, reagent grade, Fisher Chemical) were used as received without further purification. The background electrolyte solution (0.1 M KCl) was prepared using Milli-Q water (Millipore deionized, 18.2 MΩ·cm resistivity). $UO_2(NO_3)_2{\cdot}6H_2O$, $FeCl_2{\cdot}4H_2O$, and EDTA disodium salt dihydrate solid were dissolved in the electrolyte solution to prepare combinations of 1, 2, and 4 mM of U(VI), 2 mM of Fe(II), and 20 mM of EDTA solutions. The Fe(II) solution was prepared in an anaerobic glovebox using degassed Milli-Q water. The pH of the solution was adjusted using 0.1 M HCl and 0.3 M KOH solutions and measured using an Orion 111A pH meter.

The powder microelectrode (PME) was fabricated from a conventional 100 μm diameter Pt wire glass-blown electrode. After polishing the tip of the electrode, a cavity ∼40 μm deep was hand-drilled on the exposed Pt wire with a square-end miniature mill (Harvey Tool) held onto a microdrill chuck pin vise. Next, mineral particles were packed into the cavity by tapping the electrode into the mineral powder on a clean quartz glass surface. After each experiment, the electrode was sonicated first in deionized water for ∼2 min to remove mineral particles, then in 1% nitric acid solution for ∼5 min, and then in deionized water for ∼5 min to remove the nitric acid. Finally, the electrode was dried in the air before being packed with new mineral particles.

https://doi.org/10.1021/acsearthspacechem.1c00417
ACS Earth Space Chem. 2022, 6, 830−846

2.2. Electrochemistry Experiments. Electrochemical experiments were carried out using a VersaSTAT3 potentiostat (Princeton Applied Research—Ametek) with the VersaStudio 2.60.6 acquisition software. A three-electrode electrochemical cell was used with a working electrode (WE), a reference electrode (RE), and a counter electrode (CE) at room temperature. The details of the electrochemical cell can be found in the previous literature.[20] In this study, the PME was used as the working electrode with a platinum counter electrode and Ag/AgCl reference electrode. However, all voltages in this study are quoted with respect to the standard hydrogen electrode (SHE) to compare peak positions more suitably with standard reduction potentials from the literature.

For each experiment, electrolyte solutions were sparged with high-purity argon for 25 min before immersing the PME. Then, the entire cell was kept under anaerobic conditions by continuously purging the solution with argon. Twenty cycles of CV at a scan rate of 50 mV/s were run before the scans were recorded; these prescans aimed to remove oxidation products from the PME surfaces and obtain relatively stable CV curves. A set of cyclic voltammograms of uranyl redox reactions at different pH values from 5 to 3 using a pyrite electrode was carried out and is presented in Figure S2. Anodic peak A2 exhibited two different trends when the pH was decreased, which is in agreement with Yuan's study.[21] At pH = 3.5, anodic peak A2 is the most obvious. Therefore, in this study, the original solutions in all voltammetric experiments were titrated to pH = 3.5 ± 0.1.

2.3. Quantum-Mechanical Calculations. The program package Gaussian09 was used to calculate the shift of the reduction potential of the uranyl and uranyl−EDTA complex on the pyrite surface. This shift was due to differences in the adsorption energies of hexavalent and pentavalent uranyl on the pyrite surface, differences in the complexation energy by EDTA, and combinations of the two. All calculations were performed using the B3LYP hybrid functional.[56,57] The small-core SDD basis set and its corresponding pseudopotential set were used for uranium.[58] For most other elements (H, C, and O), the LANL2DZ basis and pseudopotential sets were used, but the LANL2DZdp basis set was used for S atoms to approximate polarization effects.[59] To model solvation effects, the conductor-like polarizable continuum model (CPCM)[60,61] was applied for all models.

The pyrite {100} surface was constructed by cleaving a bulk pyrite crystal model and extending the conventional unit cell to obtain a 2 × 2 supercell. By removing the periodic boundary conditions, a pyrite cluster of the size 4 × 2 × 2 was obtained; each number refers to either an Fe or a disulfide ion, resulting in a total of 48 atoms ($Fe_{16}S_{32}$). For Fe atoms on the pyrite surface, the high-spin configuration was used. There may be unpaired spins if surface steps and kink sites are considered.[39] The possible occurrence of unpaired spins in such a case would depend not only on the surface feature with its corresponding coordination number but also on whether adsorption is taking place near the Fe site. Because of the complexity of this consideration, such an analysis is beyond the scope of this study. A spin-unrestricted formalism was employed because of unpaired spins. The top layer of the surface was free to relax, while its edges and the bottom layer were fixed in their bulk position to minimize the edge effects and better approximate the underlying bulk. To evaluate the contribution of the pyrite surface and ligand ($HEDTA^{3-}$) complexation on the redox potential of uranyl, a free uranyl or uranyl−HEDTA species were put on the pyrite surface to perform geometry optimizations and frequency calculations. The latter was necessary to obtain thermodynamic properties such as the entropy and Gibbs free energy required to complete the thermodynamic cycle, as shown in Figure 1. In our calculations, free uranyl was hydrated with five water molecules in its equatorial plane, as demonstrated in previous studies, and an additional dielectric fluid surrounding this first hydration sphere.[62,63]

Reduction potential shifts were derived from the Gibbs free energies (at 298 K) of each redox pair using the Nernst equation combined with the quantum-mechanical results for each species. For the surface-adsorbed species, the reduction-potential shift due to the adsorption energy differences of species with different oxidation states onto the pyrite surface was calculated from the changes in the Gibbs free energy after the adsorption of each species using the thermodynamic cycle shown in the gray box in Figure 1. To derive Gibbs free energies in addition to the standard molecular energies that are provided in a standard quantum-mechanical approach, each calculation requires vibrational analysis using a quasi-harmonic approximation. We calculated molecular energies and vibrational terms using both Gaussian09 and DMol^3 (local density functional calculations on molecules).[64] The same pyrite cluster and uranyl models that were used for the Gaussian calculations were used in DMol^3. Atomic orbitals were described using double numerical plus d-functions (DND). Solvation effects were approximated by immersing the reactants in a dielectric fluid using COSMO (conductor-like screening model).[65] All calculations were performed using the B3LYP hybrid functional,[56,57] and core electrons were treated using the density functional theory (DFT) semicore pseudopotentials. Thermal smearing with a parameter of 0.03 Ha (0.8 eV) was applied to allow electrons to distribute more easily to their correct orbitals. In general, the combination of molecular-energy contributions from one program package with frequency terms (c_pT and $-T\Delta S$) from another is acceptable as long as the frequency contributions are obtained from the energy-optimized geometries in that respective module. The best agreement with our experimental data was obtained by combining Gaussian molecular energies and corresponding DMol^3 vibrational contributions. Thus, the peak shifts reported in this Article use this combined approach.

The thermodynamic cycle in Figure 1a describes the relationship of the reaction Gibbs free energies in homogeneous and heterogeneous (on the pyrite surface) systems. The cycle in the gray box refers to redox reactions of the free uranyl versus the surface-adsorbed uranyl, and the corresponding reactions are eqs 1−3.

$$UO_2^{2+} + e^- \rightarrow UO_2^{+} \quad \Delta G_{react} \tag{1}$$

$$\text{pyrite}{>}UO_2^{2+} + e^- \rightarrow \text{pyrite}{>}UO_2^{+} \quad \Delta G^*_{react} \tag{2}$$

$$\Delta G_{ads} = G(\text{pyrite}{>}X) - G(\text{pyrite}) - G(X) \tag{3}$$

In eqs 2 and 3, X represents any adsorbate and ">" represents the adsorption to the mineral surface. Using Figure 1a, we can calculate the potential shift of the uranyl redox potential due to the difference in adsorption energies of uranyl species with varying oxidation and complexation states onto the pyrite surface as follows,

https://doi.org/10.1021/acsearthspacechem.1c00417
ACS Earth Space Chem. 2022, 6, 830−846

$$\Delta G^*_{react} = \Delta G_{react} + \Delta(\Delta G_{react}) = \Delta G_{react} + (\Delta G_{ads,Red1} - \Delta G_{ads,Ox1}) \quad (4)$$

$$\Delta(\Delta G_{react}) = -nF\Delta V \quad (5)$$

$$\Delta V = -(\Delta G_{ads,Red} - \Delta G_{ads,Ox})/(nF) \quad (6)$$

where $\Delta G_{ads,Red}$ is the Gibbs free adsorption energy of the reduced species, $\Delta G_{ads,Ox}$ is the Gibbs free adsorption energy of the oxidized species, n is the number of transferred electrons, and F is the Faraday constant. Gibbs free adsorption energies (ΔG_{ads}) can be calculated using eq 3.

The last redox reaction outside the gray box in Figure 1a is the redox reaction of the uranyl−HEDTA complex on the pyrite surface. The peak shift due to HEDTA complexation can be calculated using the thermodynamic cycle (Figure 1a) in the same manner. The related equations are as follows,

$$\Delta G^{**}_{react} = \Delta G^*_{react} + \Delta(\Delta G^*_{react}) = \Delta G^*_{react} + (\Delta G_{ads,Red2} - \Delta G_{ads,Ox2}) \quad (7)$$

$$\Delta(\Delta G^*_{react}) = \Delta G_{ads,Red2} - \Delta G_{ads,Ox2} \quad (8)$$

In summary, the experimentally observed peak shift can be compared with the differences in Gibbs free adsorption energies of the oxidant and the reductant.

3. RESULTS

In situ electrochemical experiments and quantum-mechanical calculations were conducted to study the effect of EDTA complexation on redox reactions of uranium mediated by pyrite surfaces. First, redox reactions of pyrite in a background electrolyte only (i.e., without added uranyl or EDTA) were characterized. Then, redox reactions of uranium on pyrite surfaces were measured. Next, redox reactions with EDTA added to the solution on pyrite surfaces were studied. Finally, quantum-mechanical calculations were used to study the redox-potential shift of uranium due to the surface adsorption and EDTA complexation, and the results were compared with the experimental data.

3.1. Redox Reactions of Pyrite in a Background Electrolyte without Added EDTA or Uranyl. The first step was to demonstrate the voltammetric characteristics of the pyrite PME, which is important to differentiate the voltammetric peaks associated with uranium redox reactions from peaks coming from redox reactions of the pyrite surface. The CV of pyrite was used as the baseline for the voltammetric analysis of uranium in later sections. The voltammograms of the empty PME and the pyrite PME exposed to the background electrolyte solution at pH 3.5 are shown in Figure 2. The current of the pyrite PME was 1 order of magnitude higher than that of the empty one (see inset), which indicated some oxidation−reduction reactions occurring on the pyrite surface. The pyrite electrode could be seen as a capacitor due to its charge-storage capacity. In the CV of the pyrite PME, four anodic peaks (a0, a1, a2, and a3) and three cathodic peaks (c0, c2, and c3) were present. The a0/c0 redox couple matched exactly with the known redox reaction of free ions of Fe^{2+}/Fe^{3+} (0.771 V vs SHE). Fe^{2+}/Fe^{3+} ions were released to solution from the iron oxides on the pyrite surface during the preliminary 20 cycles of the CV experiments. The preliminary 20 cycles are shown in Figure S3. The first cycle was different

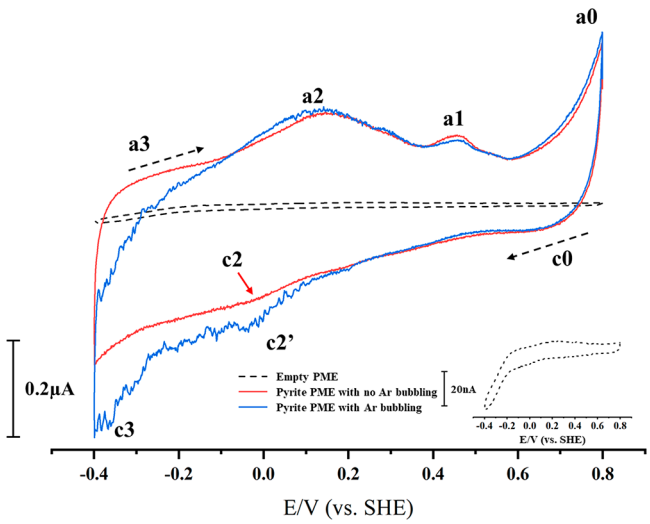


Figure 2. Cyclic voltammograms for empty PME (black dashed line) and pyrite PME without Ar bubbling (solid red line) and with Ar bubbling (solid blue line). The voltammogram of the empty PME is shown for shape comparison and also shown in the inset for clarity. Dashed arrows indicate the scan direction. The scan rate is 50 mV/s; the last of five cycles is shown.

from the final few cycles due to redox reactions of iron oxides, which came from oxidation of the pyrite surfaces exposed to air. The anodic peak a1 was attributed to the oxidation of dissolved Fe^{2+} to $Fe(OH)_3(s)$ (eq 9), which is in agreement with previous studies.[20,21] It is interesting to note that there was almost no obvious cathodic peak associated with peak a1 in the pyrite CV. This is most likely due to $Fe(OH)_3$ formed at peak a1 being unstable in a pH 3.5 solution, dissolving and dispersing into solution, and not being available at the surface for reduction.

$$Fe^{2+} + 3H_2O \rightarrow Fe(OH)_3(s) + 3H^+ + e^- \quad (9)$$

The potential applied to pyrite was incrementally increased toward more positive values during the anodic scan, which forced the pyrite surface to behave as an anode and induced the oxidation of surface-bound species. Previous studies suggested that the broad anodic peak a2 was generated by the oxidative decomposition of surface-bound species including monosulfides (S^{2-}) and S dimer (S_2^-) as well as intermediate sulfoxy anions (SO_3^{2-}, $S_2O_3^{2-}$, and SnO_2^{2-}).[66−68] The oxidative decomposition of the anodic sites of pyrite can be derived as a series of one-electron transfer steps, as shown in eqs 10a−10g.[69]

$$\text{pyrite>Fe−S−S} + H_2O \rightarrow \text{pyrite>Fe−S−SOH} + H^+ + e^- \quad (10a)$$

$$\text{pyrite>Fe−S−SOH} + H_2O \rightarrow \text{pyrite>Fe−S−S(OH)}_2 + H^+ + e^- \quad (10b)$$

$$\text{pyrite>Fe−S−S(OH)}_2 + H_2O \rightarrow \text{pyrite>Fe−S−S(OH)}_3 + H^+ + e^- \quad (10c)$$

$$\text{pyrite>Fe−S−S(OH)}_3 \rightarrow \text{pyrite>Fe−S−SO(OH)}_2 + H^+ + e^- \quad (10d)$$

https://doi.org/10.1021/acsearthspacechem.1c00417
ACS Earth Space Chem. 2022, 6, 830−846

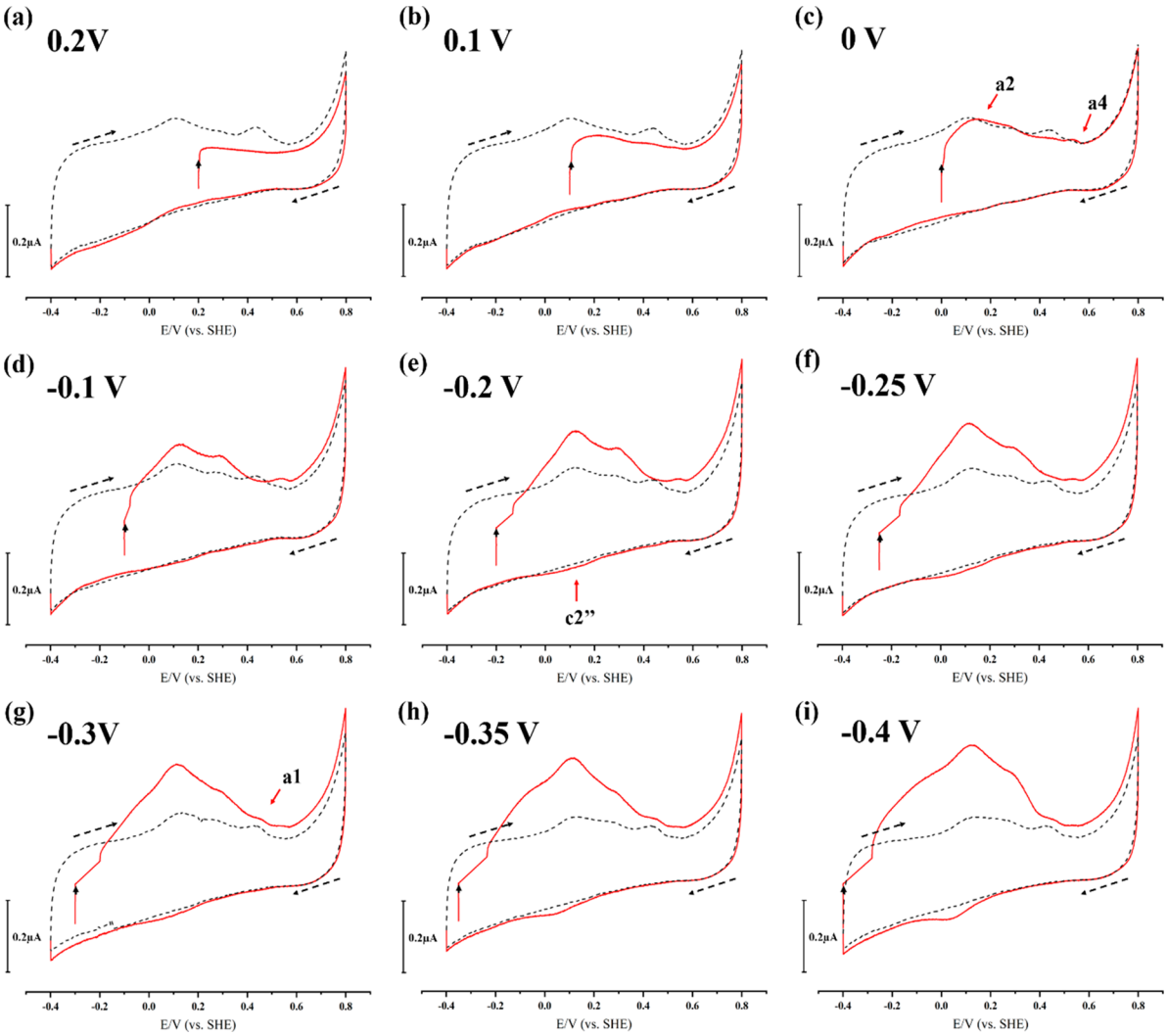


Figure 3. Cyclic voltammograms for pyrite PMEs with potential holding at (a) 0.2, (b) 0.1, (c) 0, (d) −0.1, (e) −0.2, (f) −0.25, (g) −0.3, (h) −0.35, and (i) −0.4 V for 5 min before formal CV scans. The first two cycles are shown. The solid red line is the first cycle, and the dashed black line is the second one. Dashed arrows show the scan direction. The scan rate is 50 mV/s.

$$\text{pyrite>Fe–S–SO(OH)}_2 \rightarrow \text{pyrite>Fe–S–SO}_2\text{(OH)} + \text{H}^+ + \text{e}^- \quad (10e)$$

$$\text{pyrite>Fe–S–SO}_2\text{(OH)} \rightarrow \text{pyrite>Fe–S–SO}_3 + \text{H}^+ + \text{e}^- \quad (10f)$$

$$\text{pyrite>Fe–S–SO}_3 \rightarrow \text{Fe}^{2+} + \text{S}_2\text{O}_3^{2-} + \text{e}^- \quad (10g)$$

where the notation pyrite>Fe– denotes surface-bound species.

$S_2O_3^{2-}$ is unstable in acidic solution and will transform to S and H_2SO_3 (eq 11).

$$\text{S}_2\text{O}_3^{2-} + 2\text{H}^+ \rightarrow \text{S} + \text{H}_2\text{SO}_3 \quad (11)$$

When the solution is stirred and degassed by bubbling with Ar during CV scanning, as shown in Figure 2, the currents of peaks a3 and c3 change due to the solution being stirred, and peak c2′, which is close to the electrochemical potential of peak c2, appears or its peak current increases. This behavior indicates that the process related to the couple a3/c3 and c2′ involves gaseous species. When Ar is added to the solution, hydrogen sulfide gas is released from solution. The related reactions are shown in eqs 12 and 13, which both show the release of $H_2S(g)$. S in eq 13 is derived from eq 11.

$$\text{FeS}_2 + 4\text{H}^+ + 2\text{e}^- \rightarrow \text{Fe}^{2+} + 2\text{H}_2\text{S(g)} \quad (12)$$

$$\text{S} + 2\text{H}^+ + 2\text{e}^- \rightarrow \text{H}_2\text{S(g)} \quad (13)$$

To further illustrate the attributions of redox peaks occurring on pyrite surfaces, a series of CV scans were performed after applying potential holds for 5 min at 0.2, 0.1, 0, −0.1, −0.2, −0.25, −0.3, −0.35, and −0.4 V (Figure 3). No anodic peak is visible in the first cycle until the potential hold reaches 0 V. Two anodic peaks (a2 and a4) are shown in Figure 3c. With increasing negative potential, the area under peak a2 increases. This observation agrees well with the description that peak a2 is attributed to a sequence of electron-derived reactions (eqs 10a–10g) that generate $S_2O_3^{2-}$. As the negative potential increases to −0.2 V, peak c2′′ (Figure 3e), analogous to peak c2′ (Figure 2), appears, and the peak area increases significantly from −0.2 V onward. The increase in area of peak c2″ may be related to the accumulation of $S_2O_3^{2-}$ at peak a2. Therefore, peak c2″ (or c2′) is attributed to the reduction of S (eq 13) generated by the reduction of $S_2O_3^{2-}$ (eq 11).

https://doi.org/10.1021/acsearthspacechem.1c00417
ACS Earth Space Chem. 2022, 6, 830−846

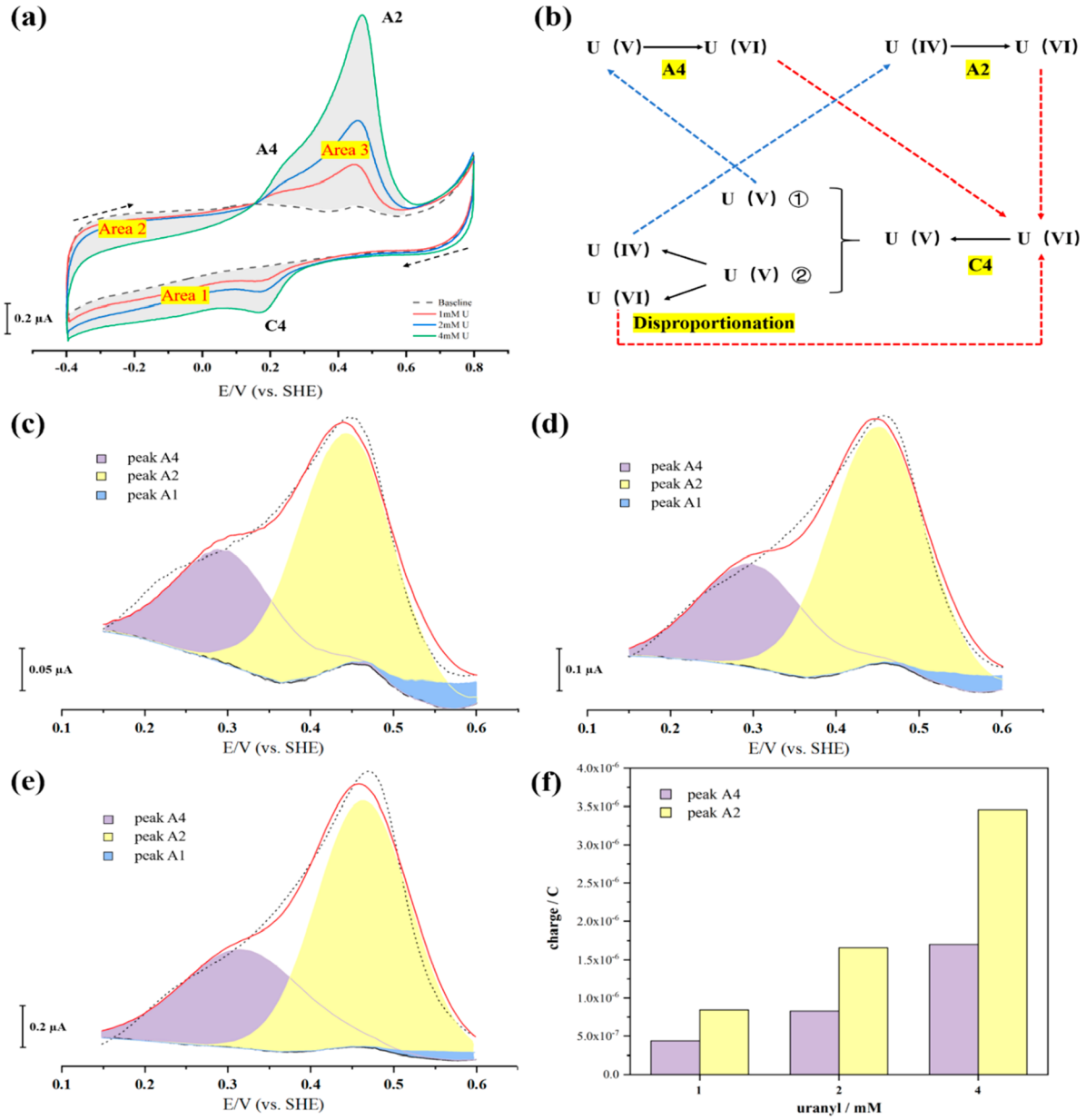


Figure 4. (a) Cyclic voltammograms for pyrite PMEs in uranyl solutions of concentrations from 1 to 4 mM. The dashed lines are the voltammograms for pyrite PMEs in a background solution containing 0.1 M KCl at pH 3.51. Dashed arrows indicate the scan direction. The scan rate is 50 mV/s; the last of five cycles is shown. (b) Reaction cycle of uranium on the pyrite electrode surface. The fitting curves of area 3 in uranyl concentrations of 1, 2, and 4 mM are shown in (c), (d), and (e), respectively. The black dashed lines are the original data, and the red solid lines are the cumulative fitting curves. (f) Peaks A4 and A2 charge bars calculated by fitting and integrating that show a proportional relationship between transferred charge and uranyl concentration.

When the negative potential is −0.3 V(Figure 3g), peak a1 appears while peak a4 disappears. Fe^{2+} is generated at low reduction potentials (eq 12), resulting in the oxidative formation of $Fe(OH)_3$ at peak a1 (eq 9). Peak a4 is assigned to the oxidation of FeS_2 to S (eq 14), which was also shown by Renock et al.[20] Finally, the formation of an $Fe(OH)_3$ layer inhibits further oxidation of FeS_2, resulting in the disappearance of peak a4.

$$FeS_2 \rightarrow Fe^{2+} + 2S + 2e^- \quad (14)$$

3.2. Redox Reactions of Uranium on the Pyrite Surface. This section discusses the studied redox reactions of uranium (starting with $U^{VI}O_2^{2+}$ in solution) on pyrite surfaces. In particular, the redox mechanism of uranium on pyrite was further evaluated using the transferred charge as determined by integrating the area under a given peak in the voltammograms. Figure 4a shows the voltammograms for pyrite PMEs with uranyl added to the solution (in addition to the background electrolyte). Additional peak pairs (C4/A4 and A2 in Figure 4a) appeared when uranyl was added, with peak A4 being a shoulder peak. Increasing currents for the cathodic and anodic peaks with increasing concentrations of $U^{VI}O_2^{2+}$ from 1 to 4 mM in solution indicated that these new peaks were associated with redox transitions of uranium. The midpoint potential of peak C4/A4 (E_{mid} = 0.2 V) on the pyrite surface was close to the standard reduction potential of UO_2^{2+}/UO_2^{+} (E^0 = 0.16 V). The difference between E_{mid} and E^0 was only 0.04 V, which was mainly the result of the

https://doi.org/10.1021/acsearthspacechem.1c00417
ACS Earth Space Chem. 2022, 6, 830−846

difference in Gibbs free adsorption energies of uranium species with different oxidation states on the pyrite surface (this shift coincided with the calculated value, 0.02 V, from the quantum-mechanical difference in adsorption energies of different oxidation states; see the Computational Results section). The reaction for the C4/A4 redox couple can be written as

$$\text{pyrite}{>}U^{V}O_2^{+} \rightarrow \text{pyrite}{>}U^{VI}O_2^{2+} + e^{-} \quad (15)$$

Peak A2 at ~0.45 V in Figure 4a was attributed to the oxidation of U(IV) (eq 16), which was formed as a result of the disproportionation of pentavalent uranium to tetra- and hexavalent ones (eq 17).[20,21] U(V) came from the reduction of uranyl on the pyrite surfaces. Yuan and Pan demonstrated, using spectroscopic and microscopic measurements, that the reduction of U(VI) proceeded first through surface-associated U(VI) to form U(V).[35,36]

$$\text{pyrite}{>}U^{4+} + 2H_2O \rightarrow \text{pyrite}{>}U^{VI}O_2^{2+} + 4H^{+} + 2e^{-} \quad (16)$$

$$2\text{pyrite}{>}U^{V}O_2^{+} + 4H^{+} \rightarrow \text{pyrite}{>}U^{4+} + \text{pyrite}{>}U^{VI}O_2^{2+} + 2H_2O \quad (17)$$

Figure 4b shows the reaction cycle of uranium on the pyrite surface. With $U^{VI}O_2^{2+}$ added to the solution, the hexavalent uranium was reduced to pentavalent uranium, which occurred at peak C4. Then a fraction of the pentavalent uranium oxidized back to hexavalent at peak A4, and the rest underwent disproportionation to produce tetravalent and hexavalent uranium. The formed tetravalent uranium oxidized in a two-electron transition to hexavalent uranium at peak A2. To confirm these reaction processes, the charges transferred under areas 1, 2, and 3 of the voltammograms in Figure 4a were calculated according to eq 18. Similarly, the voltammograms at 100 and 150 mV/s were integrated, and the transferred charges were calculated. For integrations, the voltammogram of the pyrite PME in a background solution without uranium was used as the baseline. All calculated results are shown in Table 1.

$$Q = \frac{1}{\nu}\int_{E1}^{E2} I(E)\,dE \quad (18)$$

where Q refers to the electronic charge transferred in coulombs (C), $E1$ and $E2$ refer to the two potentials marking the beginning and end of the peak in V, I refers to the current in A, and ν refers to the scan rate in V/s.

Table 1. Charges Derived from Integrating over Areas 1, 2, and 3 for Different Scan Rates and Different Uranyl Concentrations

scan rate (V/s)	uranyl concentrations (mM)	Q1 (μC)	Q2 (μC)	Q3 (μC)	(Q1 + Q2) (μC)	(Q1/Q2) (μC)
0.05	1	0.95	0.29	1.33	1.25	3.25
	2	1.82	0.59	2.56	2.41	3.08
	4	3.17	1.90	5.24	5.07	1.66
0.1	1	0.65	0.21	0.94	0.86	3.12
	2	1.22	0.43	1.78	1.66	2.84
	4	2.15	1.35	3.63	3.50	1.59
0.15	1	0.54	0.19	0.75	0.72	2.90
	2	0.96	0.40	1.40	1.37	2.39
	4	1.67	1.10	2.84	2.77	1.51

In general, reduction was considered to occur in the cathodic scan, and oxidation was considered to occur in the anodic scan. However, as shown in Table 1, $Q1 \neq Q3$, which contradicted the charge balance shown in Figure 4b. Actually, some reduction still happened at the beginning of the anodic scan as long as the voltage was below the oxidation peak A4 (up to the crossover potential that is clearly visible at 0.2 V in the anodic scan in Figure 4a). As shown in Figure 4a in area 2 (below the crossover point of the pyrite baseline and the pyrite−uranyl scan), the currents in the voltammograms of uranyl solutions were lower than the baseline of pyrite only. We interpreted the reducing currents as the reduction of some portion of hexavalent uranium. The pyrite powder packed in the electrode acted as a capacitor, which could provide electrons to the reduction reaction. As shown in Table 1, $(Q1 + Q2)$ was almost equal to $Q3$ for different scan rates and different uranyl concentrations, which confirmed our hypothesis of continuing reduction at the beginning of the anodic scan where the actual electrochemical potential was still below the standard reduction potential. As shown in area 1 of Figure 4a, the steady-state trailing cathodic current could be observed. The continuing reduction in the anodic scan and the steady-state reduction in the cathodic scan were both attributed to the reduction of the extra hexavalent uranium, which was generated continuously toward the electrode surface through the disproportionation of pentavalent uranium. In other words, the reaction rate of the disproportionation of pentavalent uranium was not fast enough to provide the hexavalent uranium toward the electrode surface in a timely manner, which resulted in the steady-state trailing cathodic current in area 1 and the anodic current under the baseline in area 2. As shown in Table 1, the ratio of $Q1/Q2$ decreased with scan rate, which showed the number of lagging charges transferred increased with scan rate. Therefore, the disproportionation was a rate-limiting step.

To quantify how much pentavalent uranium on the pyrite surface underwent disproportionation, two peaks (because the raw peak had a shoulder) were fitted to area 3 first. These fitted peaks were defined as A2 and A4 (Figure 4c−e), from which the number of charges transferred in peaks A2 and A4 could be derived. As for the peak fitting, the initial Gaussian fitting was done to make the fitting line overlap the original line. Once the fit was satisfactory for a set of peaks, the full width at half-maximum (fwhm) and the peak position were maintained to the maximum extent possible for subsequent fits. Peak A1 was the oxidation of FeS_2 to S, having been described in detail in section 3.3. Figure 4f shows the integration and calculation results of the charge transferred in peaks A2 and A4. The charge transferred in peak A2 was about twice as much as the one in peak A4 $\{q(A4) \approx 1/2q(A2)\}$. The transition of pentavalent uranium to hthe exavalent one on pyrite is shown in eq 15, with the charge transferred being $q(A4)$ and the number of moles of U oxidized being $n(\text{pyrite}{>}U^{V}) = n(A4) = q(A4)/F$. The transition of U^{IV} to U^{VI} on pyrite is shown in eq 16, with the charge transferred being $q(A2) = 2q(A4)$ and the number of moles of U oxidized being $n(\text{pyrite}{>}U^{IV}) = n(A2) = 1/2q(A2)/F \approx q(A4)/F = n(A4)$. Because no peak was observed that refers to the direct reduction of U^{V} to U^{IV}, we assumed that all tetravalent uranium was generated from the disproportionation of pentavalent uranium. Thus, the molar numbers of U^{IV} being oxidized in the anodic scan (eq 16) have to agree with the tetravalent U generated by disproportionation (eq 17). As

https://doi.org/10.1021/acsearthspacechem.1c00417
ACS Earth Space Chem. 2022, 6, 830−846

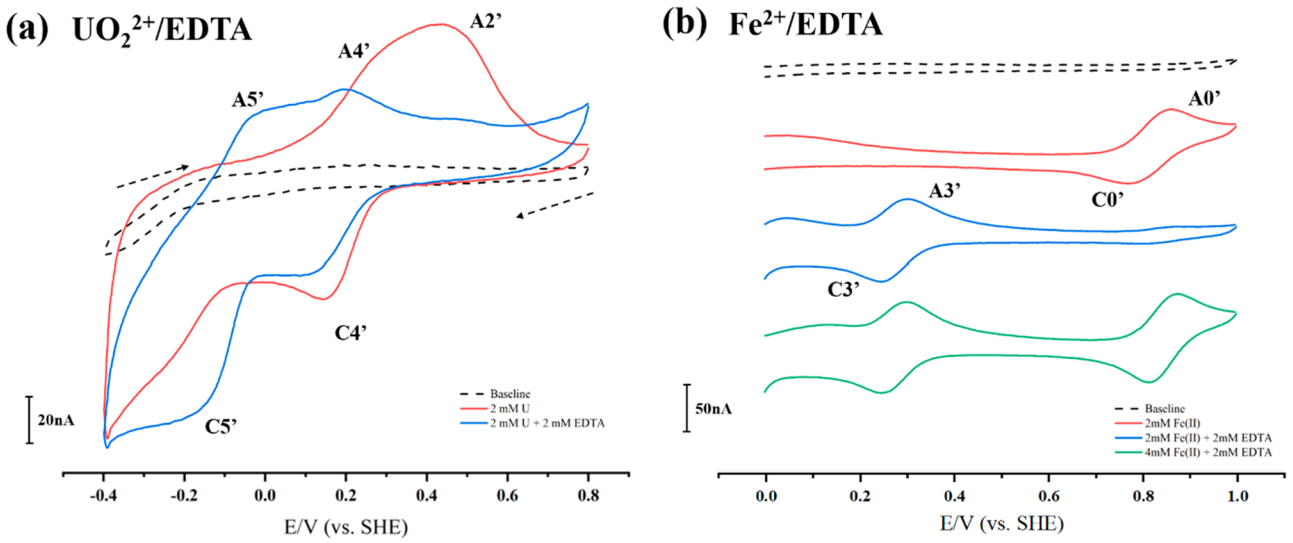


Figure 5. Cyclic voltammograms for empty PMEs for different combinations of solutions containing (a) UO_2^{2+}/EDTA and (b) Fe^{2+}/EDTA. (a) UO_2^{2+} solution (2 mM) (red solid line) and 2 mM UO_2^{2+} + 2 mM EDTA solution (blue solid line). (b) Fe^{2+} (2 mM) solution (red solid line), 2 mM Fe^{2+} + 2 mM EDTA solution (blue line), and 4 mM Fe^{2+} + 2 mM EDTA solution (green line). The dashed lines are the voltammograms in a background solution containing only 0.1 M KCl solution with pH = 3.51. Dashed arrows show the scan direction. Scan rate is 50 mV/s; the last of five cycles is shown.

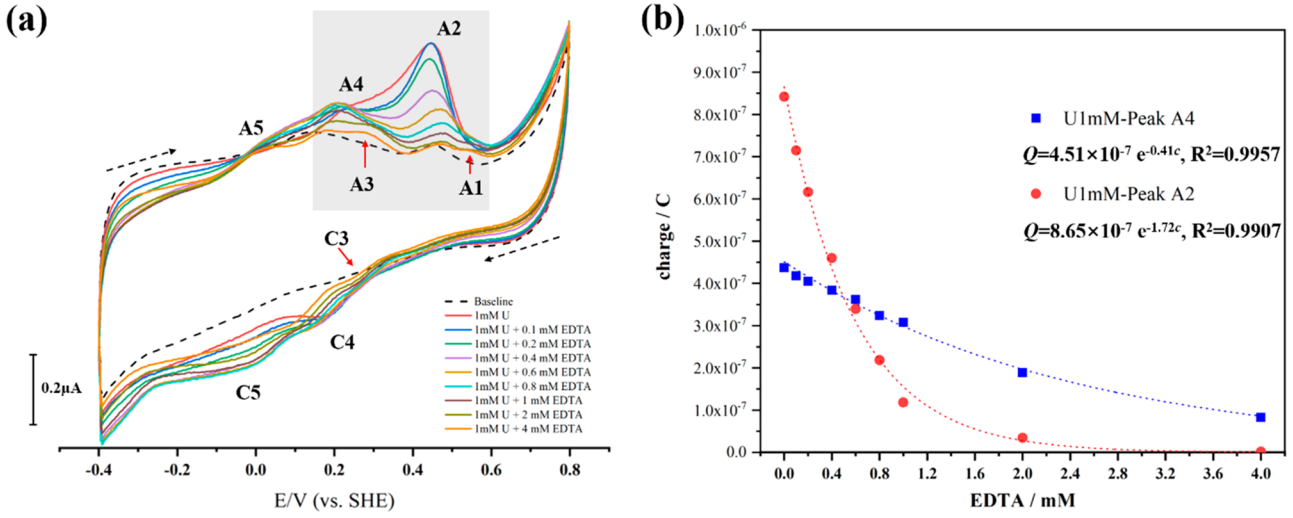


Figure 6. (a) Cyclic voltammograms for pyrite PMEs in 1 mM UO_2^{2+} solution with varying concentrations of EDTA. The dashed lines are the voltammograms for pyrite PMEs in a background solution containing 0.1 M KCl solution with pH = 3.51. The scan rate is 50 mV/s; the last of five cycles is shown. (b) Charge transferred over peaks A2 and A4 by fitting and integrating from the gray area in the left figure as a function of adding EDTA into the 1 mM UO_2^{2+} solution.

shown in eq 17, because it required 2 mol of pentavalent U to generate 1 mol of U^{IV} and 1 mol of U^{VI}, the molar numbers of pentavalent uranium $\{n'(\text{pyrite}{>}U^{V})\}$ undergoing disproportionation were twice as much as that of tetravalent uranium $\{n'(\text{pyrite}{>}U^{V}) = 2n(\text{pyrite}{>}U^{IV}) = 2n(\text{A4})\}$ being generated. The total pentavalent uranium generated in areas 1 and 2 of Figure 4a was $n_{tot}(\text{pyrite}{>}U^{V}) = n(\text{pyrite}{>}U^{V}) + n'(\text{pyrite}{>}U^{V}) = 3n(\text{A4})$. Therefore, ~2/3 of pentavalent uranium underwent disproportionation in this study.

3.3. Effect of EDTA Complexation on Redox Reactions of Uranium. The effect of EDTA complexation on redox reactions of uranium on the pyrite surface was explored, including potential shifts of uranium redox processes on pyrite surfaces due to the complex formation with EDTA and the reaction sensitivity of U(IV) and U(V) to EDTA in solution. Uranium and iron are metal ions that can form dissolved EDTA complexes in the solution of our system. To confirm the assignments of peaks to redox processes of U−EDTA and Fe−EDTA complexes, CV with an empty PME was conducted by adding UO_2^{2+}/Fe^{2+} and EDTA to the background solution, as shown in Figure 5. Figure 5a shows the cyclic voltammograms with uranyl and EDTA in solution. When 2 mM UO_2^{2+} was added without EDTA to the background electrolyte solution, a set of peaks comparable to those described in Figure 4a appeared. These were peaks A2′, A4′, and C4′. After adding 2 mM EDTA to the solution, an additional peak pair C5′/A5′ appeared, and peaks C4/A4/A2 decreased or disappeared (Figure 5a). The coupled redox peaks C5′/A5′ were interpreted to come from the redox reaction of the uranyl−EDTA complex. With $U^{VI}O_2(\text{HEDTA})^-$ being the predom-

https://doi.org/10.1021/acsearthspacechem.1c00417
ACS Earth Space Chem. 2022, 6, 830−846

inant uranyl−EDTA species at pH = 3.5 based on the speciation calculation using Visual MINTEQ (Figure S4), the reduction of this species can be written as

$$U^{VI}O_2(HEDTA)^- + e^- \rightarrow U^{V}O_2(HEDTA)^{2-} \quad (19)$$

During the electrochemical experiment, the dissolved Fe ions came from the dissolution of pyrite, especially because the strong Fe−EDTA complexes helped extract iron from the pyrite surface. As shown in Figure 5b (red line), the coupled redox peak pair C0′/A0′ was attributed to the Fe^{2+}/Fe^{3+} couple (eq 20), whose potentials are close to the c0/a0 coupled peaks in Figure 2. The addition of 2 mM EDTA to the 2 mM Fe^{2+} solution resulted in the appearance of the new peak couple C3′/A3′ while the couple C0′/A0′ almost disappeared, which was attributed to the complexation reaction between Fe and EDTA. According to the speciation calculation using Visual MINTEQ (Figure S5), the predominant complex species for Fe^{2+}−EDTA was $[Fe^{II}(EDTA)]^{2-}$. Thus, the coupled redox peaks C3′/A3′ were attributed to the redox reaction of the $Fe^{II}(EDTA)^{2-}/Fe^{III}(EDTA)^-$ couple (eq 21). When adding 2 mM EDTA to the 4 mM Fe^{2+} solution, we observed both coupled peak pairs in the same voltammogram, which showed that limited EDTA resulted in the reappearance of the Fe(III)/Fe(II) couple, alongside the Fe(III)−EDTA/Fe(II)−EDTA couple. It should be noted that the scan range in Figure 5b was from −0.4 to 1.0 V, but only the range between 0 and 1 V was shown in order to focus on the important redox couples.

$$Fe^{3+} + e^- \rightarrow Fe^{2+} \quad (20)$$

$$Fe^{III}(EDTA)^- + e^- \rightarrow Fe^{II}(EDTA)^{2-} \quad (21)$$

As shown in Figure 6a, CV with pyrite PMEs was performed with successive addition of EDTA to 1 mM uranyl solution. Electrochemistry experiments with 2 and 4 mM uranyl solutions are presented in Figures S6a and S7a. In Figure 6a, two new coupled redox peaks (C5/A5 and C3/A3) appeared after adding EDTA to the uranyl solution. The coupled peaks C5/A5 likely came from the redox reaction of the uranium−EDTA complex as the coupled redox peaks C5′/A5′ in Figure 5a had similar potential positions. However, there was a difference in the midpoint potentials between C5/A5 and C5′/A5′, potentially resulting from the different adsorption energies of uranyl complexes on pyrite and platinum surfaces (0.1 V difference). The redox reaction related to the coupled peaks C5/A5 can be expressed as eq 22. By the difference of midpoint potentials between C5/A5 and C4/A4, it was obtained that the potential shift of pyrite−U(VI)/U(V) due to complexation with EDTA was about −0.21 V (computational result was −0.29 V; see section 3.4).

$$\text{pyrite}{>}U^{VI}O_2(HEDTA)^- + e^- \rightarrow \text{pyrite}{>}U^{V}O_2(HEDTA)^{2-} \quad (22)$$

The coupled redox peaks C3/A3 shown in Figure 6a had almost the same redox potential as C3′/A3′ in Figure 5b, which were assigned to the redox reaction of the $Fe^{II}(EDTA)^{2-}/Fe^{III}(EDTA)^-$ couple. Note that, with an EDTA concentration ≥1 mM, peak A1 started to appear at ∼0.35 V (Figure 6a). According to the peak-assignment discussion in section 3.1, the potential of peak A1 was close to that of peak a4 in Figure 3c and was attributed to the oxidation of FeS_2 (eq 14, $S^{1-} \rightarrow S^0$).

First, peaks of the anodic scans from 0.15 to 0.6 V, the gray zone in Figure 6a, were fitted and integrated to obtain the areas of peaks A2 and A4. Subsequently, these peak areas were divided by the scan rates to obtain the number of electrons transferred corresponding to a specific peak. In addition, peaks A1 and A3 were included in the peak fitting. When EDTA was added to the solution, EDTA complexation of ferric iron (from the dissolution/oxidation of pyrite) inhibited the formation of an $Fe(OH)_3$ layer. Such an $Fe(OH)_3$ layer inhibited further oxidation of pyrite, and thus, adding EDTA promoted further dissolution/oxidation of pyrite. With the formation of Fe−EDTA complexes, peak A1 could be observed with EDTA added. Peak A3, whose peak potential was close to that of peak A3′ in Figure 5b, is considered to be the transition of $Fe^{II}(EDTA)^{2-} \rightarrow Fe^{III}(EDTA)^-$ (eq 21). Figure 6b shows the effect of EDTA on the charge transferred over peaks A2 and A4. As analyzed in section 3.2, peak A2 represents the oxidation of U(IV) to U(VI), and peak A4 represents the oxidation of U(V) to U(VI). Therefore, the amounts of charge transferred from U(IV)/U(V) to U(VI) decreased for both with increasing EDTA concentrations due to the complexation reaction of uranyl with EDTA. The transferred charges (Q, in C) as a function of EDTA concentration (c, in mM) are fitted using an exponential model (eq 23).

$$Q = A\ e^{-Bc} \quad (23)$$

A (reflecting the initial peak/charge transferred with no EDTA added) and B (sensitivity of charge transferred with EDTA added) are fitting parameters. The greater the value of B, the greater was the decrease of charge transferred with increasing EDTA concentration. Thus, the B value could be used to evaluate the effect of EDTA on the uranium redox reaction kinetics due to complexation. The fitting results of the curves are presented in Figure 6b. High correlation coefficients (R^2) between fitting curves and experimental data were obtained, confirming the validity of the exponential model. The B values of peak A2 (U(IV) → U(VI)) were more than twice those of peak A4 (U(V) → U(VI)) for three different concentrations of uranyl solution, which showed that the effect of EDTA for peak A2 was more pronounced than that for peak A4. The (U(IV) → U(VI)) oxidation decreased more with increasing EDTA concentration than did the (U(V) → U(VI)) oxidation. The reason may be that U(IV) was more prone to form complexes with EDTA than U(V), and then more U(IV) would get complexed and come off the pyrite surface, thus no longer being available for oxidation. Therefore, the oxidation of U(IV) was more sensitive to the presence of EDTA in solution than that of U(V).

3.4. Computational Results. Quantum-mechanical calculations, as described in the Methods section (see section 2.3), were used to quantify and understand the mechanism of EDTA complexation and adsorption onto pyrite for U species with different oxidation states. This procedure also strengthened the assignment of observed CV peaks to specific redox transitions.

For the $U^{V}O_2^+/U^{VI}O_2^{2+}$ redox pair on the pyrite surface, the redox-potential shifted by 0.02 V for the reduction on the pyrite surface from the redox potential of aqueous uranyl, according to eqs 4−6. By adding this potential shift to the standard reduction potential (SRP) of the uranyl reduction reaction (0.16 V for $U^{VI}O_2^{2+}$ to $U^{V}O_2^+$ vs SHE), the reduction potential of UO_2^{2+} on the pyrite surface was calculated to be 0.18 V (vs SHE). The result agreed well with our experimental

https://doi.org/10.1021/acsearthspacechem.1c00417
ACS Earth Space Chem. 2022, 6, 830−846

Table 2. Calculated Thermodynamics of Uranyl Species with and without HEDTA Ligand on the Pyrite Surface[a]

	calculated peak shift (DMol^3)		experimental	
reactions	vs SRP	vs reaction (a)	vs SRP	vs reaction (a)
(a) pyrite>UO_2^{2+} + e^- → pyrite>UO_2^+	0.02		0.04	
(b) pyrite>$[UO_2(HEDTA)]^-$ + e^- → pyrite>$[UO_2(HEDTA)]^{2-}$	−0.26	−0.29	−0.17	−0.21

[a]All values have units of V and are calculated using DMol^3. Peak shift values are shown relative to both the free aquo-complexed redox potential (standard reduction potential, SRP) and the surface-adsorbed uranyl.

data, with both indicating small shifts to more positive potentials, meaning the adsorption made the reduction of uranyl more favorable on the pyrite surface (Table 2).

One reason why there may be differences between experimentally observed potential shifts and calculated ones is that the calculated shifts to a certain degree are dependent on the computational parameters used, such as density functional, basis set, or pseudopotentials. In addition, the treatment of spin−orbit coupling (SOC) code also has an effect. While hexavalent uranium does not have SOC because there are no unpaired spins, pentavalent uranium does gain energy due to SOC (−0.31 eV for the uranyl reduction reaction from U(VI) to U(V)[70] in solution). However, the potential shift would only be affected by changes in SOC of the difference of redox species with varying oxidation states (i.e., the difference of the difference in SOC). Thus, the effect of SOC cancels out for the most part. In addition, experimentally observed and calculated potential shifts are highly sensitive to local charge environments. Thus, changes in the concentration and chemical composition of background electrolytes typically lead to shifts in peak positions. These effects of local charge environments could potentially be treated using the different protonation states. However, this complexity is beyond the scope of this Article.

When the uranyl species were complexed with HEDTA, our electrochemical experiment showed a peak shift to a more negative value for the uranyl−HEDTA redox potential. The redox potential shift of the surface-adsorbed uranyl−HEDTA relative to the complex-free uranyl species could be calculated by comparing the Gibbs free energies of the redox reactions for each reaction (e.g., redox reaction of aqueous uranyl and redox reaction of uranyl−HEDTA on the pyrite surface). The calculation followed the thermodynamic cycle shown in Figure 1a and eqs 7 and 8 in the Methods section. The calculated value showed a peak shift to a more negative potential (−0.29 V, Table 2) relative to the surface-adsorbed uranyl reduction. Compared to the reduction of free aqueous uranyl, there was a difference of −0.26 V to more negative potentials. The shift of reduction potential to a more negative value (in both the experiment and the calculation) indicated a less favorable reduction in the presence of HEDTA ligand.

In addition to variations in the calculated shift of the electrochemical potential due to the parameters addressed earlier, one has to keep in mind that adsorption in the actual experiment is likely a mixture of adsorption to flat terrace sites as well as to step edges, kinks, and defect sites. The thermodynamic entities of adsorption and hydration are also dependent on the exact hydration mechanism. While the combination of using explicit water molecules for the first hydration sphere and adding dielectric fluid surrounding this hydrated setup is typically the most reliable approximation to derive solvation energies computationally, variations in this hydration scheme would also lead to variations in the calculated potential energy shifts.

4. DISCUSSION

Generally, the overall redox reaction occurring at an interface is controlled by multiple processes, including diffusion, adsorption, and chemical reactions, where electron transfer can potentially occur. In section 3.2, we showed that disproportionation of U(V) is the rate-limiting step controlling electron transfer. In section 3.3, we found that the U(IV) reaction is more sensitive to EDTA in solution than that of U(V). Here, we further discuss the effect of EDTA complexation on the subprocesses involved in the uranium redox reactions, including diffusion and adsorption. Due to the steady-state trailing current in the cathodic peak, it is hard to separate the reduction of initial $U^{VI}O_2^{2+}$ from that generated by the disproportionation. We have confirmed the electron balance during one voltammogram in section 3.2 $\{(Q1 + Q2) \approx Q3\}$, and the oxidation peaks of uranium have been fitted well. Therefore, the anodic peaks (the gray zone shown in Figure 6a) will be used to evaluate the effect of EDTA complexation on electron transfer.

4.1. Diffusion. There are different ways to analyze electrochemical data in order to determine if the kinetics of the redox process is predominantly diffusion-controlled. One such method uses the theoretical relation between current and time for linear diffusion, which is described by the Cottrell equation,[64,65,56]

$$i(t) = \frac{nFAD_0^{1/2}C_0}{\pi^{1/2}t^{1/2}} \tag{24}$$

where $i(t)$ is the current at time t, n is the number of electrons transferred over one redox peak, F is the Faraday constant, A is the reactive surface area, D_0 is the diffusion coefficient, C_0 is the initial concentration of free uranyl in the bulk solution, and t is the time.

For the cyclic voltammogram,

$$E(t) = E_1 + \nu t \tag{25}$$

where $E(t)$ is the potential at time t, E_1 is the initial potential, ν is the scan rate, and t is the time.

Substitution of eqs 24 and 25 into eq 18 gives

$$Q = \frac{2nFAD_0^{1/2}C_0(E_2 - E_1)^{1/2}}{\pi^{1/2}} \cdot \nu^{-1/2} \tag{26}$$

where E_2 is the end potential, E_1 and E_2 are fixed values, and accordingly, $\frac{2nFAD_0^{1/2}C_0(E_2 - E_1)^{1/2}}{\pi^{1/2}}$ is a constant for the same charge-transfer process. Therefore, Q is a function of $\nu^{-1/2}$ for a diffusion-controlled process; conversely, if for a given species and consistent experimental conditions but varying scan speeds the charge of a given peak is proportional to the inverse of the square of the scan speed, then the kinetics of the overall redox process is largely diffusion-controlled.

Figure 7 shows the relationship between the transferred charge and the scan rate in 1 mM UO_2^{2+} solutions with varying

https://doi.org/10.1021/acsearthspacechem.1c00417
ACS Earth Space Chem. 2022, 6, 830−846

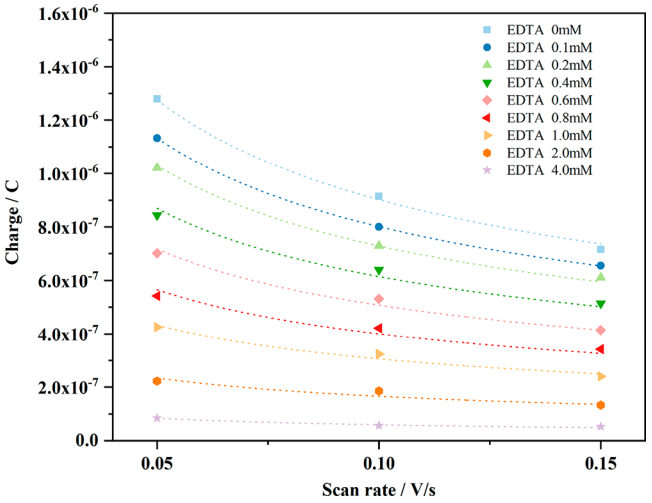


Figure 7. Charge transferred as derived from integrating over the anodic peak (relative to the background without added uranyl) in the range from 0.15 to 0.6 V as a function of scan rate in 1 mM UO_2^{2+} solutions with varying concentrations of EDTA.

EDTA concentrations. To compare the effect of EDTA on the charge-transfer process, the curves in Figure 7 are fitted by using eq 27. High correlation coefficients (R^2, all exceed 0.98) confirm the validity of the model described in eq 27. In eq 27, a is the fitting constant, which is equal to $\frac{2nFAD_0^{1/2}C_0(E_2-E_1)^{1/2}}{\pi^{1/2}}$, derived from eq 26. Therefore, the diffusion coefficients can be calculated using eq 28. Fitting constants a and diffusion coefficients D_0 for varying EDTA concentrations in 1 mM UO_2^{2+} solution are presented in Table 3.

$$Q = av^{-1/2} \tag{27}$$

$$D_0 = \left(\frac{a\pi^{1/2}}{2nFAC_0(E_2 - E_1)^{1/2}}\right)^2 \tag{28}$$

Table 3. Fitting Constants a and Diffusion Coefficients D_0 for Varying EDTA Concentrations in 1 mM UO_2^{2+} Solution

EDTA (mM)	free uranyl[a] (mM)	a ($\times 10^{-7}$ C·(V/s)$^{1/2}$)	D_0 ($\times 10^{-9}$ m^2/s)
0	0.906	2.85	0.07
0.1	0.746	2.53	0.08
0.2	0.591	2.30	0.12
0.4	0.318	1.94	0.30
0.6	0.142	1.60	1.15
0.8	0.064	1.26	3.93
1	0.033	0.97	10.49
2	0.007	0.53	78.48
4	0.003	0.19	83.28

[a]The free uranyl concentrations with the addition of different amounts of EDTA were obtained from speciation calculations using Visual MINTEQ.

where Q is the total charge transferred over peaks A2 and A4 obtained by fitting in section 3.3. Because the oxidation over peak A2 undergoes two-electron transition {U(IV) → U(VI)} and the oxidation over peak A4 undergoes one-electron transition {U(V) → U(VI)}, the number of transferred electrons n is the weighted average of electron numbers transferred over the two reactions, where the relative weights are their peak areas. The reactive surface area A has been calculated as shown in the Supporting Information.

To further confirm the effect of EDTA complexation on the kinetics of the redox process controlled by diffusion, the mean square diffusion displacement of free uranyl going to the pyrite surface is calculated as follows,[71]

$$\langle x \rangle = (q_t D_0 t)^{1/2} \tag{29}$$

where $\langle x \rangle$ is the mean diffusion distance that the uranyl molecule diffuses in a given amount of time t, which is equal to the scan time from 0.15 to 0.6 V for a given scan rate. Using eq 29 and the calculated D_0, we can determine $\langle x \rangle$ for uranyl with different EDTA concentrations and scan rates. As shown in Figure 8, a hemispherical diffusion model can be used to

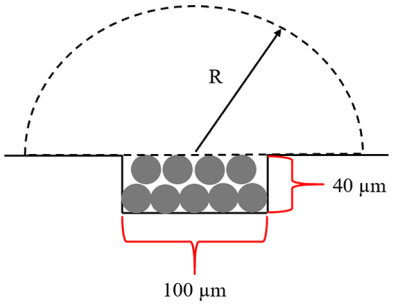


Figure 8. Diagram for the hemispherical diffusion model.

describe the range (reactive volume) in which free uranyl can undergo electron transfer to produce a particular redox peak. Uranium species inside this range can undergo redox reactions that are not possible outside the range. The transferred charges in the hemispherical model to produce oxidation peaks can be expressed as follows,

$$Q = \frac{2\pi R^3 C_0 N_A e n}{3} \tag{30}$$

where R is the hemispherical radius, C_0 is the concentration of free uranyl in the bulk solution, N_A is Avogadro's constant (equal to 6.022×10^{23}/mol), e is the elementary charge (1.602×10^{-19} C), and n is the number of electrons transferred over the oxidation peaks. R can be derived from the concentration of free uranyl and the total charge over the oxidation peaks, as shown in eq 31.

$$R = \left(\frac{3Q}{2\pi C_0 N_A e n}\right)^{1/3} \tag{31}$$

The electron transfer (ET) occurring at the solution−pyrite interface is ultimately dependent on the relation between the mean diffusion distance $\langle x \rangle$ and the radius R in the hemispherical diffusion model. If $\langle x \rangle < R$, the overall reaction is diffusion-limited, while diffusion is less of a limiting factor when $\langle x \rangle > R$. The calculated $\langle x \rangle$ and R values for varying EDTA concentrations in 1 mM UO_2^{2+} solution at different scan rates are shown in Table 4. Most of the x values are smaller than R, so it is hard to get enough charges inside the reactive volume to produce the oxidation peaks that we see. Consequently, the ET occurring at the pyrite−solution interface is diffusion-limited. With 0.05 V/s of scan rate, when the EDTA concentration in the solution is >0.8 mM, $\langle x \rangle$

https://doi.org/10.1021/acsearthspacechem.1c00417
ACS Earth Space Chem. 2022, 6, 830−846

Table 4. $\langle x \rangle$ and R Values for Varying EDTA Concentrations in 1 mM UO_2^{2+} Solution with Different Scan Rates[a]

	scan rate (V/s)					
	0.05		0.10		0.15	
EDTA concentration (mM)	$\langle x \rangle$	R (μm)	$\langle x \rangle$	R (μm)	$\langle x \rangle$	R (μm)
0	61	162	43	144	35	133
0.1	67	167	48	148	39	139
0.2	79	175	56	156	45	147
0.4	128	204	90	186	74	173
0.6	249	256	176	233	144	215
0.8	**461**	**312**	**326**	**287**	266	268
1	**753**	**369**	**532**	**337**	**435**	**305**
2	**2059**	**510**	**1456**	**479**	**1189**	**429**
4	**2121**	**532**	**1500**	**467**	**1224**	**456**

[a]The values where $\langle x \rangle > R$ are bolded.

is larger than R, which indicates an ET process that is less diffusion-limited. If the scan rate increases to 0.15 V/s, more EDTA (1 mM) needs to be added to the solution to keep diffusion from becoming a limiting factor to ET. Therefore, the addition of EDTA promotes the delivery of uranyl from the bulk solution to the reaction interface.

4.2. Adsorption. To understand the adsorption characteristics of uranyl (with or without complexation) onto pyrite, two commonly used isotherms, Langmuir and Freundlich, are used to fit the experimental data. We are not strictly measuring the adsorption amount of uranium on the pyrite surface, but rather the number of electrons transferred during the time that the voltammetry experiment takes to sweep over a redox peak of uranium is used as an indirect indicator. The number of transferred electrons is quantified by the peak area divided by the scan rate and used to replace the adsorption amount. Thus, there are some caveats about using adsorption isotherms in this context. First, this is not just adsorption but rather the combination of adsorption and a redox reaction. Second, we are not assuming that equilibrium is reached during the time that the experiment takes to sweep over a given redox peak. Nevertheless, insights into the adsorption mechanism can still be gained from this approach because the electrons transferred over the redox peak are proportional to the amount of uranyl adsorbed. Using the formalism of adsorption isotherms—even though, rather than an equilibrium, it is only the number of ions that adsorb and transfer electrons while sweeping over a peak—helps one to identify that increasing uranyl concentration leads to saturation, as evident by the more successful use of the Langmuir isotherm. Although not perfect, this model helps describe and possibly explain what occurs at the pyrite surface during the redox process.

In the Langmuir model, it is assumed that there is only a monomolecular layer on the surface and no subsequent interactions among adsorbed molecules,[72] which means that there is no stacking of adsorbed molecules. This implies that the absorption site on the surface will converge to a maximum adsorption amount, called S_{max}. The Freundlich isotherm does not have this restriction. It is often used to describe adsorption on heterogeneous surfaces.[73] The two model equations can be defined as follows.

The Freundlich model is

$$q_e = K_f C_e^{1/n} \tag{32}$$

where q_e is the transferred electron in C, C_e is the equilibrium concentration of UO_2^{2+} in solution, and K_f and n are Freundlich constants that correspond to adsorption capacity and adsorption intensity, respectively. $n = 1$ means that the adsorption is linear. $n > 1$ suggests that some initial adsorption favors more adsorption, which means that strong favorable interactions exist between the adsorbents and adsorbates.

The Langmuir model is

$$q_e = S_{max} C_e / (1/k_l + C_e) \tag{33}$$

where S_{max} and k_l are Langmuir constants. k_l is related to the affinity of binding sites. In the Langmuir model, it is assumed that, at maximum coverage, there is only a monomolecular layer on the surface. Thus, S_{max} represents the maximum monolayer adsorption capacity. For small concentration values, i.e., $k_l C_e \ll 1$, the Langmuir and Freundlich models are the same for $n = 1$ in the Freundlich model. In highly concentrated systems, i.e., $k_l C_e \gg 1$, the adsorbed amount q_e asymptotically approaches S_{max}.

The fitting Freundlich and Langmuir plots are presented in Figure 9. As can be seen from the results, the Freundlich model fits well with high correlation coefficients ($R^2 \geq 0.991$) compared to the Langmuir model ($R^2 \leq 0.944$). This suggests that there is multilayer adsorption occurring at the pyrite surface. Using adsorption experiments, some researchers have identified uranyl monolayers on pyrite surfaces.[74,12] However, in contrast to our experiments, the presence of an electric field is not a factor in simple adsorption scenarios, although reduction still occurs. In electrochemical experiments, both the adsorption layer and the electron transfer differ from those associated with uranyl adsorption alone. In addition, reduction of uranyl can lead to the formation of uraninite-like nanoparticles on the surface.[36,75−77] For the three scan rates (Figure 9), all n values for the Freundlich isotherm fitting are higher than unity, indicating that uranyl adsorption promotes further adsorption.

5. SUMMARY AND CONCLUSIONS

This study investigates the redox reaction of uranium mediated by pyrite surfaces and the effect of EDTA complexation using electrochemical methods and quantum-mechanical calculations. In the voltammograms of the powdered-pyrite electrode, the reduction potential of UO_2^{2+}/UO_2^{+} is 0.2 V. Compared to the standard reduction potential of uranyl, there is a 0.04 V shift to a more positive potential due to the difference in surface adsorption adsorption energies of the two species with different oxidation states. The potential shift of the pyrite−U(VI)/U(V) transition due to complexation with EDTA is about −0.21 V, with similar results from the quantum-mechanical calculations. Many studies indicate that the pathway more likely to produce U(IV) than direct reduction is where UO_2^{2+} is first reduced to UO_2^{+}, followed by the formation of U(IV) through the disproportionation of two UO_2^{+} ions.[20,21,78,79] Herein, we found that disproportionation is the rate-limiting step for the redox reaction of uranium, which results in a steady-state cathodic current and continued reduction after the reversal scan. Also, we quantified that ∼2/3 of pentavalent uranium generated by the reduction of hexavalent uranyl undergoes disproportionation on the pyrite surface. By adding different amounts of EDTA to obtain

https://doi.org/10.1021/acsearthspacechem.1c00417
ACS Earth Space Chem. 2022, 6, 830−846

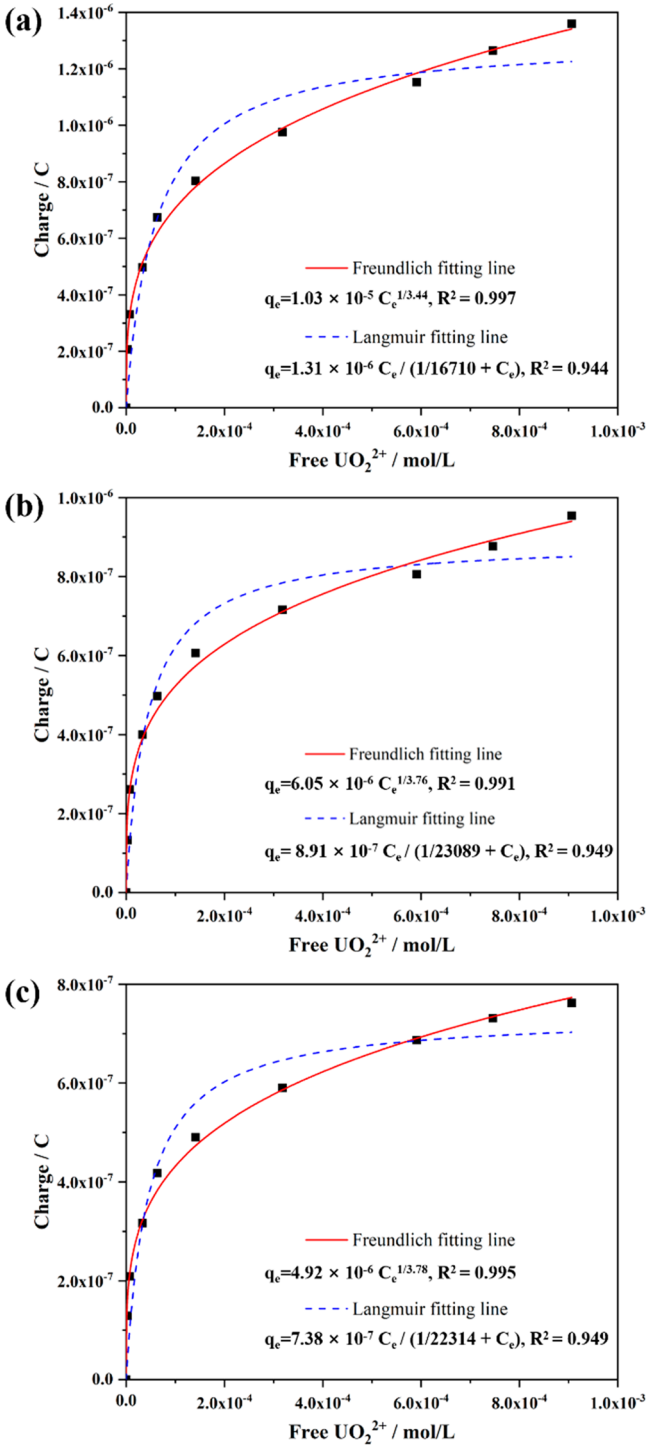


Figure 9. Transferred charges as a function of free UO_2^{2+} with 0.1−4 mM of EDTA added to the 1 mM uranyl solution at scan rates of (a) 50, (b) 100, and (c) 150 mV/s.

different concentrations of free uranyl and changing the scan rate, we obtained the relationship between the charge transferred over the redox peak of uranium and the scan rate. Further, the effect of EDTA complexation on the subprocesses involved in the uranium redox reactions, including diffusion and adsorption, has been explored. Although previous studies have investigated the effect of EDTA on the mobilization of environmental uranium, including the adsorption and redox reactions of uranium on mineral surfaces, few studies have differentiated the subprocesses. Adding EDTA to the uranyl solution promotes the delivery of free uranyl from the bulk solution to the reaction interface, such that the electron-transfer process become less diffusion-limited. It was speculated that EDTA played a role as a transport agent in uranyl delivery. According to the results of the thermodynamics analysis, the adsorption of uranyl onto pyrite surfaces in the gradient electric field is multimolecular layer adsorption, through which electron transfer can occur.

Our study's approach is fundamentally different from previous studies in that, by using a pyrite-powder microelectrode, we can control the surface potential (and, thus, oxidation states) of the reactive surface of pyrite and evaluate uranium redox processes occurring in situ under various solution conditions. Thereby, we can simulate different redox conditions of uranium in natural subsurface environments. In addition, the findings of this study are crucial in understanding the redox behavior of uranyl in the presence of EDTA and developing a deeper understanding of uranium immobilization by mineral surfaces. Ongoing experiments are focusing on using complementary analytical techniques (surface spectroscopy, electron microscopy, etc.) to further validate and expand some of these findings.

■ ASSOCIATED CONTENT

Supporting Information

The Supporting Information is available free of charge at https://pubs.acs.org/doi/10.1021/acsearthspacechem.1c00417.

Calculation process of the reactive surface area, XRD patterns, cyclic voltammograms, and speciation of dissolved UO_2^{2+} and dissolved Fe^{2+} as a function of pH (PDF)

■ AUTHOR INFORMATION

Corresponding Author

Udo Becker − *Department of Earth and Environmental Sciences, University of Michigan, Ann Arbor, Michigan 48109, United States;* orcid.org/0000-0002-1550-0484; Email: ubecker@umich.edu

Authors

Yingwei Wang − *Department of Earth and Environmental Sciences, University of Michigan, Ann Arbor, Michigan 48109, United States; School of Chemical Engineering and Technology, China University of Mining and Technology, Xuzhou, Jiangsu 221116, P. R. China;* orcid.org/0000-0003-3043-550X

Sooyeon Kim − *Department of Earth and Environmental Sciences, University of Michigan, Ann Arbor, Michigan 48109, United States;* orcid.org/0000-0001-9413-068X

Maria C. Marcano − *Department of Earth and Environmental Sciences, University of Michigan, Ann Arbor, Michigan 48109, United States;* orcid.org/0000-0002-7476-5925

Yijun Cao − *School of Chemical Engineering, Zhengzhou University, Zhengzhou, Henan 450001, P. R. China*

Complete contact information is available at: https://pubs.acs.org/10.1021/acsearthspacechem.1c00417

Notes

The authors declare no competing financial interest.

■ ACKNOWLEDGMENTS

This research was funded by the U.S. National Science Foundation, Division of Earth Sciences, Grant no. EAR-1223976. Y.W. is grateful to the China Scholarship Council for financially supporting his research at the University of Michigan.

■ REFERENCES

(1) Means, J. L.; Crerar, D. A.; Duguid, J. O. Migration of radioactive wastes: radionuclide mobilization by complexing agents. *Science* **1978**, *200* (4349), 1477−1481.
(2) Sillanpää, M. Environmental fate of EDTA and DTPA. In *Reviews of environmental contamination and toxicology*; Springer: 1997; pp 85−111.
(3) Alder, A. C.; Siegrist, H.; Gujer, W.; Giger, W. Behaviour of NTA and EDTA in biological wastewater treatment. *Water Res.* **1990**, *24* (6), 733−742.
(4) Pirkanniemi, K.; Metsärinne, S.; Sillanpää, M. Degradation of EDTA and novel complexing agents in pulp and paper mill process and waste waters by Fenton's reagent. *Journal of hazardous materials* **2007**, *147* (1−2), 556−561.
(5) Hinck, M.; Ferguson, J.; Puhaakka, J. Resistance of EDTA and DTPA to aerobic biodegradation. *Water Sci. Technol.* **1997**, *35* (2−3), 25.
(6) Seshadri, H.; Sinha, P. Efficient decomposition of liquid waste containing EDTA by advanced oxidation nanotechnology. *Journal of Radioanalytical and Nuclear Chemistry* **2012**, *292* (2), 829−835.
(7) Cross, J. E.; Ewart, F. T.; Greenfield, B. F. Modelling the behaviour of organic degradation products. *MRS Proc.* **1988**, *127*, 715−722.
(8) Francis, A.; Dodge, C. Microbial mobilization of plutonium and other actinides from contaminated soil. *Journal of environmental radioactivity* **2015**, *150*, 277−285.
(9) Rihs, S.; Sturchio, N. C.; Orlandini, K.; Cheng, L.; Teng, H.; Fenter, P.; Bedzyk, M. J. Interaction of uranyl with calcite in the presence of EDTA. *Environ. Sci. Technol.* **2004**, *38* (19), 5078−5086.
(10) Gephart, R. E.; Lundgren, R. E. *Hanford tank cleanup: a guide to understanding the technical issues*; Office of Scientific and Technical Information, U.S. Department of Energy: 1998; DOI: 10.2172/195769.
(11) Read, D.; Ross, D.; Sims, R. The migration of uranium through Clashach Sandstone: the role of low molecular weight organics in enhancing radionuclide transport. *Journal of Contaminant Hydrology* **1998**, *35* (1−3), 235−248.
(12) Liu, H.; Zhu, Y.; Xu, B.; Li, P.; Sun, Y.; Chen, T. Mechanical investigation of U (VI) on pyrrhotite by batch, EXAFS and modeling techniques. *Journal of hazardous materials* **2017**, *322*, 488−498.
(13) Sun, Y.; Li, J.; Wang, X. The retention of uranium and europium onto sepiolite investigated by macroscopic, spectroscopic and modeling techniques. *Geochim. Cosmochim. Acta* **2014**, *140*, 621−643.
(14) Mehta, V. S.; Maillot, F.; Wang, Z.; Catalano, J. G.; Giammar, D. E. Effect of co-solutes on the products and solubility of uranium (VI) precipitated with phosphate. *Chem. Geol.* **2014**, *364*, 66−75.
(15) Atta-Fynn, R.; Johnson, D. F.; Bylaska, E. J.; Ilton, E. S.; Schenter, G. K.; De Jong, W. A. Structure and hydrolysis of the U (IV), U (V), and U (VI) aqua ions from ab initio molecular simulations. *Inorganic chemistry* **2012**, *51* (5), 3016−3024.
(16) Chen, A.; Shang, C.; Shao, J.; Zhang, J.; Huang, H. The application of iron-based technologies in uranium remediation: A review. *Sci. Total Environ.* **2017**, *575*, 1291−1306.
(17) Qiu, S.; Lai, H.-F.; Roberson, M.; Hunt, M.; Amrhein, C.; Giancarlo, L.; Flynn, G.; Yarmoff, J. Removal of contaminants from aqueous solution by reaction with iron surfaces. *Langmuir* **2000**, *16* (5), 2230−2236.
(18) Du, X.; Boonchayaanant, B.; Wu, W.-M.; Fendorf, S.; Bargar, J.; Criddle, C. S. Reduction of uranium (VI) by soluble iron (II) conforms with thermodynamic predictions. *Environ. Sci. Technol.* **2011**, *45* (11), 4718−4725.
(19) Troyer, L. D.; Tang, Y.; Borch, T. Simultaneous reduction of arsenic (V) and uranium (VI) by mackinawite: role of uranyl arsenate precipitate formation. *Environ. Sci. Technol.* **2014**, *48* (24), 14326−14334.
(20) Renock, D.; Mueller, M.; Yuan, K.; Ewing, R. C.; Becker, U. The energetics and kinetics of uranyl reduction on pyrite, hematite, and magnetite surfaces: A powder microelectrode study. *Geochim. Cosmochim. Acta* **2013**, *118*, 56−71.
(21) Yuan, K.; Renock, D.; Ewing, R. C.; Becker, U. Uranium reduction on magnetite: Probing for pentavalent uranium using electrochemical methods. *Geochim. Cosmochim. Acta* **2015**, *156*, 194−206.
(22) Cowie, B. E.; Purkis, J. M.; Austin, J.; Love, J. B.; Arnold, P. L. Thermal and photochemical reduction and functionalization chemistry of the uranyl dication, $[U(VI)O_2]^{2+}$. *Chem. Rev.* **2019**, *119* (18), 10595−10637.
(23) Ilton, E. S.; Boily, J.-F.; Buck, E. C.; Skomurski, F. N.; Rosso, K. M.; Cahill, C. L.; Bargar, J. R.; Felmy, A. R. Influence of dynamical conditions on the reduction of U(VI) at the magnetite− solution interface. *Environ. Sci. Technol.* **2010**, *44* (1), 170−176.
(24) Ilton, E. S.; Pacheco, J. S. L.; Bargar, J. R.; Shi, Z.; Liu, J.; Kovarik, L.; Engelhard, M. H.; Felmy, A. R. Reduction of U(VI) incorporated in the structure of hematite. *Environ. Sci. Technol.* **2012**, *46* (17), 9428−9436.
(25) Skomurski, F. N.; Ilton, E. S.; Engelhard, M. H.; Arey, B. W.; Rosso, K. M. Heterogeneous reduction of U6+ by structural Fe2+ from theory and experiment. *Geochim. Cosmochim. Acta* **2011**, *75* (22), 7277−7290.
(26) Ilton, E. S.; Haiduc, A.; Cahill, C. L.; Felmy, A. R. Mica surfaces stabilize pentavalent uranium. *Inorganic chemistry* **2005**, *44* (9), 2986−2988.
(27) Roberts, H. E.; Morris, K.; Law, G. T.; Mosselmans, J. F. W.; Bots, P.; Kvashnina, K.; Shaw, S. Uranium (V) incorporation mechanisms and stability in Fe (II)/Fe (III)(oxyhydr) oxides. *Environmental Science & Technology Letters* **2017**, *4* (10), 421−426.
(28) Arumugam, K.; Becker, U. Computational redox potential predictions: applications to inorganic and organic aqueous complexes, and complexes adsorbed to mineral surfaces. *Minerals* **2014**, *4* (2), 345−387.
(29) Kim, S.; Becker, U. Diffusion Kinetics of Adsorbed Species on Pyrite Surfaces. *ACS Earth and Space Chemistry* **2021**, *5* (9), 2356−2371.
(30) Becker, U.; Rosso, K. M.; Hochella, M. F., Jr The proximity effect on semiconducting mineral surfaces: a new aspect of mineral surface reactivity and surface complexation theory? *Geochim. Cosmochim. Acta* **2001**, *65* (16), 2641−2649.
(31) Rosso, K. M.; Becker, U. Proximity effects on semiconducting mineral surfaces II:: Distance dependence of indirect interactions. *Geochimica et cosmochimica acta* **2003**, *67* (5), 941−953.
(32) Walker, S. M.; Marcano, M. C.; Bender, W. M.; Becker, U. Imaging the reduction of chromium (VI) on magnetite surfaces using in situ electrochemical AFM. *Chem. Geol.* **2016**, *429*, 60−74.
(33) Kim, Y.; Yuan, K.; Ellis, B. R.; Becker, U. Redox reactions of selenium as catalyzed by magnetite: Lessons learned from using electrochemistry and spectroscopic methods. *Geochim. Cosmochim. Acta* **2017**, *199*, 304−323.
(34) Renock, D.; Becker, U. A first principles study of the oxidation energetics and kinetics of realgar. *Geochim. Cosmochim. Acta* **2010**, *74* (15), 4266−4284.
(35) Yuan, K.; Ilton, E. S.; Antonio, M. R.; Li, Z.; Cook, P. J.; Becker, U. Electrochemical and spectroscopic evidence on the one-electron reduction of U (VI) to U (V) on magnetite. *Environ. Sci. Technol.* **2015**, *49* (10), 6206−6213.
(36) Pan, Z.; Bártová, B.; LaGrange, T.; Butorin, S. M.; Hyatt, N. C.; Stennett, M. C.; Kvashnina, K. O.; Bernier-Latmani, R. Nanoscale mechanism of UO 2 formation through uranium reduction by magnetite. *Nat. Commun.* **2020**, *11*, 4001.

(37) Kang, M.; Chen, F.; Wu, S.; Yang, Y.; Bruggeman, C.; Charlet, L. Effect of pH on aqueous Se (IV) reduction by pyrite. *Environ. Sci. Technol.* **2011**, *45* (7), 2704−2710.
(38) Tu, Z.; Wan, J.; Guo, C.; Fan, C.; Zhang, T.; Lu, G.; Reinfelder, J. R.; Dang, Z. Electrochemical oxidation of pyrite in pH 2 electrolyte. *Electrochim. Acta* **2017**, *239*, 25−35.
(39) Arumugam, K.; Renock, D.; Becker, U. The basis for reevaluating the reactivity of pyrite surfaces: spin states and crystal field d-orbital splitting energies of bulk, terrace, edge, and corner Fe (II) ions. *Phys. Chem. Chem. Phys.* **2019**, *21* (12), 6415−6431.
(40) Luo, W.; Gu, B. Dissolution of uranium-bearing minerals and mobilization of uranium by organic ligands in a biologically reduced sediment. *Environ. Sci. Technol.* **2011**, *45* (7), 2994−2999.
(41) Zhao, D.; Zhang, Q.; Xuan, H.; Chen, Y.; Zhang, K.; Feng, S.; Alsaedi, A.; Hayat, T.; Chen, C. EDTA functionalized Fe3O4/graphene oxide for efficient removal of U (VI) from aqueous solutions. *J. Colloid Interface Sci.* **2017**, *506*, 300−307.
(42) Pshinko, G.; Kosorukov, A.; Puzyrnaya, L.; Goncharuk, V. Layered double hydroxides intercalated with EDTA as effective sorbents for U (VI) recovery from wastewater. *Radiochemistry* **2011**, *53* (3), 303.
(43) Kim, Y.; Marcano, M. C.; Ellis, B. R.; Becker, U. Photocatalytic reduction of uranyl: Effects of organic ligands and UV light wavelengths. *Am. J. Sci.* **2018**, *318* (9), 949−968.
(44) Kim, Y.; Marcano, M. C.; Kim, S.; Becker, U. Reduction of uranyl and uranyl-organic complexes mediated by magnetite and ilmenite: A combined electrochemical AFM and DFT study. *Geochim. Cosmochim. Acta* **2021**, *293*, 127−141.
(45) Cerrillos, C.; Ollis, D. F. Photocatalytic reduction and removal of uranium from a uranium-EDTA solution. *Journal of Advanced Oxidation Technologies* **1998**, *3* (2), 167−173.
(46) Sheng, L.; Szymanowski, J.; Fein, J. B. The effects of uranium speciation on the rate of U (VI) reduction by Shewanella oneidensis MR-1. *Geochim. Cosmochim. Acta* **2011**, *75* (12), 3558−3567.
(47) Liger, E.; Charlet, L.; Van Cappellen, P. Surface catalysis of uranium (VI) reduction by iron (II). *Geochim. Cosmochim. Acta* **1999**, *63* (19−20), 2939−2955.
(48) Jeon, B.-H.; Dempsey, B. A.; Burgos, W. D.; Barnett, M. O.; Roden, E. E. Chemical reduction of U (VI) by Fe (II) at the solid−water interface using natural and synthetic Fe (III) oxides. *Environ. Sci. Technol.* **2005**, *39* (15), 5642−5649.
(49) Zeng, H.; Giammar, D. E. U (VI) reduction by Fe (II) on hematite nanoparticles. *J. Nanopart. Res.* **2011**, *13* (9), 3741−3754.
(50) Bender, W. M.; Becker, U. Determining the kinetics of discrete aqueous redox reaction sub-steps using computational methods: Application to reactions of plutonyl (PuO2+/2+) with Fe2+, Fe3+, and hydroxyl radical (• OH). *Am. J. Sci.* **2018**, *318* (9), 893−920.
(51) Taylor, S.; Becker, U.; Rosso, K. Electron transfer pathways facilitating U (VI) reduction by Fe (II) on Al-vs Fe-oxides. *J. Phys. Chem. C* **2017**, *121* (36), 19887−19903.
(52) Taylor, S.; Marcano, M.; Becker, U. A first principles investigation of electron transfer between Fe (II) and U (VI) on insulating Al-vs. semiconducting Fe-oxide surfaces via the proximity effect. *Geochim. Cosmochim. Acta* **2017**, *197*, 305−322.
(53) Bender, W. M.; Becker, U. Resolving the kinetics of individual aqueous reaction steps of actinyl (AnO2+ and AnO22+; An= U, Np, and Pu) tricarbonate complexes with ferrous iron and hydrogen sulfide from first principles. *Radiochim. Acta* **2020**, *108* (3), 165−184.
(54) Taylor, S.; Marcano, M.; Rosso, K. M.; Becker, U. An experimental and ab initio study on the abiotic reduction of uranyl by ferrous iron. *Geochim. Cosmochim. Acta* **2015**, *156*, 154−172.
(55) Cook, P.; Kim, Y.; Yuan, K.; Marcano, M. C.; Becker, U. Electrochemical, Spectroscopic, and Computational Investigations on Redox Reactions of Selenium Species on Galena Surfaces. *Minerals* **2019**, *9* (7), 437.
(56) Raghavachari, K. Perspective on "Density functional thermochemistry. III. The role of exact exchange". *Theor. Chem. Acc.* **2000**, *103* (3−4), 361−363.
(57) Stephens, P. J.; Devlin, F. J.; Chabalowski, C. F.; Frisch, M. J. Ab initio calculation of vibrational absorption and circular dichroism spectra using density functional force fields. *J. Phys. Chem.* **1994**, *98* (45), 11623−11627.
(58) Dunning, T. H., Jr.; Hay, P. J. *Modern theoretical chemistry*; Springer: 1976.
(59) Dunning, T. H., Jr Gaussian basis sets for use in correlated molecular calculations. I. The atoms boron through neon and hydrogen. *J. Chem. Phys.* **1989**, *90* (2), 1007−1023.
(60) Cossi, M.; Rega, N.; Scalmani, G.; Barone, V. Energies, structures, and electronic properties of molecules in solution with the C-PCM solvation model. *Journal of computational chemistry* **2003**, *24* (6), 669−681.
(61) Tomasi, J.; Mennucci, B.; Cammi, R. Quantum mechanical continuum solvation models. *Chem. Rev.* **2005**, *105* (8), 2999−3094.
(62) Hagberg, D.; Karlström, G.; Roos, B. O.; Gagliardi, L. The coordination of uranyl in water: a combined quantum chemical and molecular simulation study. *J. Am. Chem. Soc.* **2005**, *127* (41), 14250−14256.
(63) Sémon, L.; Boehme, C.; Billard, I.; Hennig, C.; Lützenkirchen, K.; Reich, T.; Roßberg, A.; Rossini, I.; Wipff, G. Do perchlorate and triflate anions bind to the uranyl cation in an acidic aqueous medium? A combined EXAFS and quantum mechanical investigation. *ChemPhysChem* **2001**, *2* (10), 591−598.
(64) Delley, B. DMol, a standard tool for density functional calculations: review and advances. In *Theoretical and computational chemistry*; Elsevier: 1995; Vol. *2*, pp 221−254.
(65) Klamt, A.; Schüürmann, G. COSMO: a new approach to dielectric screening in solvents with explicit expressions for the screening energy and its gradient. *J. Chem. Soc., Perkin Trans.* **1993**, *2* (5), 799−805.
(66) Kelsall, G.; Yin, Q.; Vaughan, D.; England, K.; Brandon, N. Electrochemical oxidation of pyrite (FeS2) in aqueous electrolytes. *J. Electroanal. Chem.* **1999**, *471* (2), 116−125.
(67) Yin, Q.; Kelsall, G.; Vaughan, D.; Welham, N. Rotating Ring (Pt)−Disc (FeS2) Electrode Behavior in Hydrochloric Solutions. *J. Colloid Interface Sci.* **1999**, *210* (2), 375−383.
(68) Rimstidt, J. D.; Vaughan, D. J. Pyrite oxidation: a state-of-the-art assessment of the reaction mechanism. *Geochimica et Cosmochimica acta* **2003**, *67* (5), 873−880.
(69) Tabelin, C. B.; Veerawattananun, S.; Ito, M.; Hiroyoshi, N.; Igarashi, T. Pyrite oxidation in the presence of hematite and alumina: II. Effects on the cathodic and anodic half-cell reactions. *Science of The Total Environment* **2017**, *581*, 126−135.
(70) Hay, P. J.; Martin, R. L.; Schreckenbach, G. Theoretical studies of the properties and solution chemistry of AnO22+ and AnO2+ aquo complexes for An= U, Np, and Pu. *J. Phys. Chem. A* **2000**, *104* (26), 6259−6270.
(71) Berg, H. C. *Random walks in biology*; Princeton University Press: 2018.
(72) Aksu, Z.; Açıkel, Ü.; Kabasakal, E.; Tezer, S. Equilibrium modelling of individual and simultaneous biosorption of chromium (VI) and nickel (II) onto dried activated sludge. *Water Res.* **2002**, *36* (12), 3063−3073.
(73) Li, Y.-H.; Di, Z.; Ding, J.; Wu, D.; Luan, Z.; Zhu, Y. Adsorption thermodynamic, kinetic and desorption studies of Pb2+ on carbon nanotubes. *Water research* **2005**, *39* (4), 605−609.
(74) Luo, M.; Liu, S.; Li, J.; Luo, F.; Lin, H.; Yao, P. Uranium sorption characteristics onto synthesized pyrite. *Journal of Radioanalytical and Nuclear Chemistry* **2016**, *307* (1), 305−312.
(75) O'Loughlin, E. J.; Kelly, S. D.; Kemner, K. M. XAFS investigation of the interactions of UVI with secondary mineralization products from the bioreduction of FeIII oxides. *Environ. Sci. Technol.* **2010**, *44* (5), 1656−1661.
(76) Fox, P. M.; Davis, J. A.; Kukkadapu, R.; Singer, D. M.; Bargar, J.; Williams, K. H. Abiotic U (VI) reduction by sorbed Fe (II) on natural sediments. *Geochimica et cosmochimica acta* **2013**, *117*, 266−282.

(77) Singer, D. M.; Chatman, S. M.; Ilton, E. S.; Rosso, K. M.; Banfield, J. F.; Waychunas, G. A. U (VI) sorption and reduction kinetics on the magnetite (111) surface. *Environ. Sci. Technol.* **2012**, *46* (7), 3821−3830.
(78) Steele, H.; Taylor, R. J. A theoretical study of the inner-sphere disproportionation reaction mechanism of the pentavalent actinyl ions. *Inorganic chemistry* **2007**, *46* (16), 6311−6318.
(79) Kern, D.; Orlemann, E. The potential of the uranium (V), uranium (VI) couple and the kinetics of uranium (V) disproportionation in perchlorate media. *J. Am. Chem. Soc.* **1949**, *71* (6), 2102−2106.

Recommended by ACS

Role of Manganese Oxides in Controlling Subsurface Metals and Radionuclides Mobility: A Review
Ilana Szlamkowicz, Vasileios Anagnostopoulos, *et al.*
DECEMBER 09, 2022
ACS EARTH AND SPACE CHEMISTRY
READ

Fossil Bioapatites with Extremely High Concentrations of Rare Earth Elements and Yttrium from Deep-Sea Pelagic Sediments
Alain Manceau, Andrea Koschinsky, *et al.*
JULY 14, 2022
ACS EARTH AND SPACE CHEMISTRY
READ

Pentavalent Uranium Enriched Mineral Surface under Electrochemically Controlled Reducing Environments
Ke Yuan, Udo Becker, *et al.*
MARCH 18, 2022
ACS EARTH AND SPACE CHEMISTRY
READ

Plutonium Co-precipitation with Calcite
Enrica Balboni, Mavrik Zavarin, *et al.*
NOVEMBER 15, 2021
ACS EARTH AND SPACE CHEMISTRY
READ

Get More Suggestions >

https://doi.org/10.1021/acsearthspacechem.1c00417
ACS Earth Space Chem. 2022, 6, 830−846